Science Advances
AAAS
Manuscript Template

Photoreception and Signaling in Bacterial Phytochrome Revealed by Single Particle Cryo-EM

short title: cryo-EM structures explain light signaling

Authors: Tek Narsingh Malla[1,2], Carolina Hernandez[3], Srinivasan Muniyappan[1], David Menendez[4], Dorina Bizhga[4], Joshua H. Mendez[3], Peter Schwander[1], Emina A. Stojković[4]* and Marius Schmidt[1]*

Affiliations:

[1]Department of Physics, University of Wisconsin-Milwaukee, Milwaukee, WI 53211

[2]Present Address: Cancer Research Technology Program, Leidos Biomedical Research, Inc., Frederick National Laboratory for Cancer Research, Frederick, MD 21702, USA

[3]New York Structural Biology Center (NYSBC), New York, NY 10027

[4]Department of Biology, Northeastern Illinois University, Chicago, IL 60625

*corresponding authors: e-stojkovic@neiu.edu; smarius@uwm.edu

Abstract:

Phytochromes are red-light photoreceptors discovered in plants with homologs in bacteria and fungi that regulate a variety of physiological responses. They display a reversible photocycle between two distinct states: a red-light absorbing Pr and a far-red light absorbing Pfr state. The photoconversion regulates the activity of an enzymatic domain, usually a histidine kinase (HK). The molecular mechanism that explains how light controls the HK activity is not understood because structures of unmodified bacterial phytochromes with HK activity are missing. Here, we report three cryo-EM structures of a wild-type bacterial phytochrome with HK activity determined as Pr and Pfr homodimers and as a Pr/Pfr heterodimer with individual subunits in distinct states. We propose that the Pr/Pfr heterodimer is a physiologically relevant signal transduction intermediate. Our results offer insight into the molecular mechanism that controls the enzymatic

activity of the HK as part of a bacterial two-component system that perceives and transduces light signals.

One sentence summary:

Cryo-EM structures of a phytochrome reveal a heterodimer and explain red light-perception in non-photosynthetic bacteria.

MAIN TEXT

Introduction

The ability to sense and respond to changing environmental conditions is essential to the survival of living organisms. In bacteria and archaea, environmental signals are typically sensed through a two-component signaling mechanism composed of a histidine kinase (HK) and a response regulator (RR) (*1*). Two-component systems are highly modular and have been adapted into a variety of cellular signaling circuits. The phytochrome photoreceptors in bacteria are part of such a signaling mechanism responding to changes in the spectrum, the intensity, and the direction of light (*2*). In addition, phytochromes are ubiquitous among plants and widespread in fungi (*3, 4*). Plant phytochromes such as PhyA and PhyB that feature a C-terminal histidine kinase like domain (HKLD) have a different domain composition in comparison to bacterial phytochromes (Fig. 1 A,B) and rather unusual homodimer structures, recently revealed by cryo-EM (*5, 6*). Upon light activation plant Phys migrate to the nucleus where they induce responses such as germination, greening and shade avoiding (*7*) in a mechanism distinct from the bacterial two-component system (*8*). In photosynthetic bacteria, phytochromes stimulate various responses such as the synthesis of light-harvesting complexes (*3, 9, 10*). In non-photosynthetic bacteria their role varies from gene transfer in *Agrobacterium fabrum* (*tumefaciens*) (*11*) to multicellular fruiting body formation in myxobacteria (*12-14*). Here, we reveal structural details of the phytochrome-mediated two-component system in the non-photosynthetic myxobacterium *Stigmatella aurantiaca* (*15*) by single

particle cryo-EM. Myxobacteria are distinguished among prokaryotes by a multicellular stage in their life cycle known as fruiting bodies. In *S. aurantiaca,* fruiting body formation is controlled by red and far-red light, implicating bacteriophytochrome (BphP) signaling (*13, 16, 17*). Myxobacteria are also extensively studied for the synthesis of secondary metabolites with potential anticancer and antimicrobial properties, recently discovered to be modified by light (*18, 19*).

BphPs consists of a photosensory core module (PCM) and an output effector module (OM) (Fig. 1A). The PCM is composed of three domains: PAS (Per-Arndt-Sim), GAF (cGMP phosphodiesterase/adenylyl cyclase/FhIA), and PHY (phytochrome-specific GAF-related). The central chromophore, biliverdin (BV) (Fig. 1C), is a heme-derived, open-chain tetrapyrrole (pyrrole rings A–D) that is covalently bound through its 3" position (Fig. 1C) to an N-terminal conserved cysteine (Cys13). The C-terminal OM differs among species, although a HK domain is the most common (*3, 20, 21*). *S. aurantica* has two BphPs, SaBphP1 (*13*) and SaBphP2 (*15*) with the same domain composition including a HK domain (Fig. 1A), although HK activity has not been experimentally demonstrated. Light-dependent HK activity was found for BphPs such as the *Rhodopseudomonas palustris* RpBphP2 and RpBphP3 (*22*). Other BphPs, for example the IsPadC of *Idiomarina sepc.* (*23*) has a diguanylyl-cyclase OM, and the *Deinococcus radiodurans* DrBphP has phosphatase activity (*24*) (Fig. 1B).

BphPs interconvert between a red-light absorbing Pr state and a far red-light absorbing Pfr state, through several intermediates (Fig. 1C,D) (*14*). Upon illumination with red light (λ = 640 nm), the BV isomerizes from an all-*Z* to a *ZZE* configuration. During the isomerization, BV ring D rotates about the C_{15}= C_{16} double bond located between the pyrrole rings C and D (Fig. 1C). This drives the phytochrome into the first half of the photocycle (*25-28*). The sensory tongue of the PHY domain (Fig. 1A) shifts between a β-strand conformation in the Pr and an α-helical conformation in the Pfr state as demonstrated by several structural and spectroscopic studies (*24, 25, 27-29*).

In intact BphPs, the signal is transmitted over ~100 Å from the BV-bound chromophore binding pocket to the OM. Specifically, it is unclear how the light-regulated HK activity is controlled since near atomic resolution structures of wild-type BphPs with HK activity are missing. A sequence of amino acid residues called the PRXSF motif (*30, 31*) located in the sensory tongue as part of the PHY domain plays an important role in the Pr to Pfr transition, and henceforth in the sensing of light. The Arg of the PRXSF motif forms a key salt bridge with Asp of the PASDIP motif (*32*) of the GAF domain (that houses the BV, Fig. 1A) in the dark-adapted Pr state; see Woitowich et al. (*13*) for a partial sequence alignment. This Arg-Asp salt bridge is broken upon the β-strand to α-helix conformational change in the Pfr state (Fig. 1B). In the dark, the PCMs of several BphPs undergo thermal reversion to the Pr-state at different rates from minutes to hours, making structural studies that involve the crystallization of the Pfr state challenging (*25*). A recent cryo-EM study of the DrBphP-RR chimera demonstrated structural changes of the sensory tongue from the Pr to Pfr state in the phytochrome photoreceptor with OM, albeit the fusion to a RR (*24*).

Crystal structures of the SaBphP1 and SaBphP2 PCMs were determined in the Pr state and offered the first insight into light-sensing enzymes of myxobacteria (*13, 15*). Both proteins crystallized as homodimers similar to the PCM crystal structures of the DrBphP in the Pr and Pfr states (*25, 27*), that of bathy phytochrome PaBphP with Pfr as the dark-adapted state (*33*) and that of plant PhyB in the Pr state (*34*). Notably, one of the crystal structures of the full-length BphP from *Idiomarina spec.* with modifications in the linker region connecting the PCM to the diguanylyl cyclase domain was determined as a Pr/Pfr heterodimer (*35*). Given the lack of structures of complete, unmodified photoreceptors in distinct Pr and Pfr states, we focused on using cryo-EM to determine the corresponding structures of the wild-type SaBphP2, which is a canonical BphP and more stable than the SaBphP1. The cryo-EM structures of the wild-type SaBphP2 as presented here offer direct insight into a Pr/Pfr heterodimer as an important intermediate in the photocycle and

draw conclusions on the red-light signaling mechanism in non-photosynthetic bacteria and in two-component systems.

Results

1.1 The histidine kinase activity of SaBphP2

We determined the spectra of three distinguishable species for the intact SaBphP2 and the corresponding PCM (Fig. 2A,B). The spectrum with the absorption maximum at 705 nm represents the Pr state, that with a strong shoulder at 756 nm corresponds to the Pfr state (see also Fig. 1B). Absorption spectra with a weaker far-red shoulder than that of the Pfr state (black lines in Fig. 2A,B) are obtained upon exposure of the protein to ambient white light. The Pr state is stable for an extended period of time, whereas the Pfr state undergoes slow dark reversion (on the order of hours) to Pr for both intact and truncated (PCM) constructs (Fig. 2A,B). We further establish that the SaBphP2 has HK activity by means of radioactive labeling with ATP [γ-^{32}P] regardless of the light conditions used during the autophosphorylation reaction (Fig. 2C). The HK activity of the enzyme in the pure Pr state is higher than that of the enzyme in the Pfr state (Fig. 2D).

The absorption spectra relate to structures of SaBphP2 with and without the HK domains with corresponding cryo-EM maps determined at near atomic resolution. Details of single particle cryo-EM map reconstruction and structure determination are comprehensively listed in the supplementary material (SM) (figs. S1 – S4). A general flow chart for cryo-EM data processing is shown in fig. S1. The cryo-EM structures of this canonical wild-type bacterial phytochrome reveal conformational changes between different signaling states of the reversible Pr/Pfr photocycle and provide concrete structural evidence for the mechanism of light-induced signal transduction.

1.2 The structure of the homodimer in the Pr state

To capture the structure of wild-type SaBphP2 in the Pr state, we irradiated the protein solution with 740 nm light before it was applied to the cryo-EM grid (see the SM). The structure of the homodimer in the Pr state is shown in Fig. 3A together with the corresponding cryo-EM map.

126 The PCM portion of the map as well as part of the linker to the HK domain (up to residue 538)
127 were interpreted with a structural model (green ribbons). The structure of the PCM part is
128 essentially identical to the published high-resolution crystal structure of the same protein (*15*),
129 shown by the orange ribbon overlaid on subunit A (Fig. 3A). The dimer interface of both PCM and
130 the linker region to the HK domain, is composed of two long α-helices,

131 The sensory tongue of the PHY domain, in both subunits of the Pr state, is a two stranded β-
132 sheet which is also observed in the crystal structure of SaBphP2 PCM and other homologous BphPs
133 in the Pr state. The length of the sensory tongue, measured by the distance between Glu469 and
134 Pro456 is ~31 Å (Fig. 4D). The BV chromophore is in the all-Z configuration with ring D forming
135 hydrogen bond with the conserved His275 of the GAF domain (Fig. 4A). The BV is further
136 stabilized by additional conserved residues also shown in Fig. 4A. The conserved Asp192 and
137 His245 are forming H-bonds with pyrrole rings A and C, respectively. The propionate of ring B is
138 connected by hydrogen bonds to the conserved Tyr201 and Arg239, and that of ring C to Arg207,
139 Ser257 and Ser259. As expected, the salt-bridge between Arg457 of the PRXSF motif in the sensory
140 tongue and Asp192 of the PASDIP motif in the GAF domain is observed. The conserved pyrrole
141 water near pyrrole rings A, B and C which has been observed in high-resolution crystal structures
142 of the PCM of SaBphP2 and related BphPs (*15, 36*) in the Pr state was not resolved in the map.

143 A simplified view of the SaBphP2 dimer can be obtained by displaying the dimer interface
144 helices which are shown in Fig. 5 in dark green (subunit A) and pink (subunit B). The linker helices
145 to the HK domain are shown by a lighter shade of green and pink, respectively. In the Pr state, both
146 the dimer helices and the linker helices cross each other within the PHY domain. The top positions
147 of the dimer interface helices are ~25 Å apart (Fig. 5A,G). The PAS and PHY domains are separated
148 by 39 Å and 22 Å, respectively (Fig. 5A,D). Fig. 6 provides a different view on the relative
149 orientation of the SaBphP2 structural domains. When measured with respect to the PAS domain,

150 the GAF domain is oriented at an angle of 55˚, the PHY domain at 60˚ and the HK domain at 35˚
151 (Fig. 6A,D) .

152 **1.3 The structure of the homodimer in the Pfr state**

153 We obtained the structure of the full length SaBphP2 homodimer in the Pfr state (Fig. 3C)
154 after irradiating the protein solution with 660 nm light (Fig. 2A). The β-strands of the sensory
155 tongue move apart in both subunits (Fig. 4D,E). The strand (containing the PRXSF motif) that
156 returns from the BV pocket to the PHY domain has changed to an α-helix. The length of the sensory
157 tongue is now shorter (23 Å, Fig. 4D,E). The network of hydrogen bonds formed between the BV
158 and neighboring conserved amino acids in the GAF domain (Fig. 4B) differs extensively from the
159 Pr state due to large conformational changes and the reorientation of the BV chromophore (fig. S5).
160 Ring D no longer forms hydrogen bond with the conserved His275 due to the Z/E isomerization
161 about the C_{15}=C_{16} bond and the corresponding ~180° rotation of ring D (compare Fig. 4A and B).
162 Notably, the salt bridge between the Asp192-Arg457 is broken as a result of the conformational
163 transition of the sensory tongue to an α-helix. A hydrogen bond between Asp192 and Ser459 of the
164 PRXSF motif is formed (Fig. 4B).

165 The helices at the dimer interface helices are parallel to each other (Fig. 5F, Fig. 6I). The PAS
166 domains are pulled closer by ~7 Å and the PHY domains are pushed apart by more than 10 Å
167 compared to the homodimer in the Pr state. The pivot point of the domain displacements between
168 homodimers in the Pr and Pfr states is located within the GAF domain (Fig. 5G,H,I). The GAF and
169 PHY domain orientations change by ~30˚ and the HK by ~65˚ in relation to the Pr state (compare
170 Fig. 6D with F). The coiled linkers straighten up. However, the long linker helices display a kink
171 near Phe485 in both subunits (arrows in Fig. 5F, Fig. 6I, fig. S6). These structural disruptions cause
172 the rotation of the HK. In addition to the strongly rotated conformation, an alternate orientation of
173 the HK is observed which is placed at an angle similar to that determined in the Pr state (Fig. 6D,F
174 and fig. S5C).

1.4 The structure of the Pr/Pfr heterodimer

In addition to the two homodimers described above, we determined the structure of a SaBphP2 heterodimer after the protein was exposed to weak ambient white light (Fig. 2A and Fig. 3B). Within the heterodimer, called the Pr/Pfr heterodimer in the following, one subunit is in the Pr and the other in the Pfr state. In fact, a large portion (> 90 %) of the protein molecules on the cryo-EM grid is present in the heterodimeric form and the rest as homodimers in the Pfr state. Within the PCM region, the cryo-EM map is resolved to ~ 3 Å (fig. S1) while the map features within the HK region are resolved at ~9 Å resolution (fig. S1). The map reveals the overall shape of the HK (Fig. 3) much better than either of the homodimers determined in the Pr and Pfr states, respectively. The SaBphP2 HK structure is consistent with the previously determined crystal structure of a truncated, cytoplasmic portion of a sensor HK (*37*) (fig. S6B). Features in the HK region become more pronounced after local refinement in *cryoSPARC (38)* (fig. S1). The backbone structure of the HK can be modeled and refined in this map (Fig. 3B, fig. S1, fig. S6B). Since the linker helices cross each other, the HK lobes are located on top of the PCM regions of the opposite subunits (Fig. 3B). The structure of subunit A is similar to that of the Pr state with the BV in the Z-configuration and the sensory tongue in the β-sheet conformation. Likewise, in subunit B the structures of the BV and the sensory tongue resemble those observed in the Pfr state. Within the PCM region the overall domain orientations of the Pr/Pfr heterodimer are equivalent to those of the homodimer in the Pfr state (Fig. 5E,F). The dimer interface helices are parallel and the relative orientations of the PAS, GAF and PHY domains are essentially the same in the two structures (Fig. 6E,F). The structures of the coiled coil linker and the HK, however, differ in comparison to the homodimers in both the Pr and Pfr states. As the linker helices start to unwind upon photoexcitation, the intersection point of the linker helices shifts by ~50 Å towards the HK (Fig. 6H) in the Pr/Pfr heterodimer when compared to its location in the Pr state homodimer (Fig. 6G). A kink appears in the linker helix near Phe485 of subunit A only, which notably is in the Pr state (Fig. 5E, Fig. 6H, fig. S6C). This

kink is absent in both subunits of the Pr homodimer. Despite the structural changes of the PCM, the HK itself does not rotate and its orientation remains close to that of the homodimer in the Pr state (Fig. 6D,E).

1.5 Structures of the SaBphP2 PCM lacking the HK domain

We obtained two cryo-EM structures of the truncated SaBphP2 PCM lacking the HK domain after exposure of the protein solution to 660 nm light or to ambient white light. With 660 nm light illumination the PCM formed a homodimer with both subunits in the Pfr state whereas exposure to ambient white light resulted in a heterodimer composed of individual subunits in distinct Pr and Pfr conformations. The structures are shown in Fig. 4C and 4F, respectively. The overall resolution (~4.5 Å) is lower than that of the corresponding PCM region (~3 Å) in the full-length SaBphP2 structures (table S1) which can be partially ascribed to the smaller size of the PCM (~110 kDa versus ~160 kDa of the intact SaBphP2). The structures of the PCM homodimer and that of the heterodimer are essentially identical to those of the corresponding PCM regions within the full-length SaBphP2; see Fig. 4C as an example.

Discussion

Our results provide detailed structural insight into the signaling pathway of the non-photosynthetic myxobacteria mediated by BphP HK activity. Based on the presented cryo-EM structures of the *S. aurantiaca* BphP2, we outline a sequence of events that characterize the path of the light signal from central BV chromophore to the HK domain, more than 100 Å in distance (Fig. 3B). Starting from the SaBphP2 homodimer in the Pr state, the absorption of a photon causes the BV chromophore in one of the subunits (subunit B in Fig. 3B and Fig. 5E) to undergo *Z* to *E* isomerization. The rotation of the BV ring D causes substantial rearrangement of the entire network of hydrogen bonds between BV and the chromophore binding GAF domain (Fig. 4B), and results in the transition of one of the β strands to an α-helix in the PHY domain's sensory tongue (Fig. 3B).

These structural changes are followed by substantial domain rotations (Fig. 6E) which destabilize the coiled linker. A kink forms in the linker helix of the opposite subunit (subunit A in Fig. 5E), which is still in the Pr state. As a result of the kink, the HK tilts (to the left in Fig. 3B) and one HK lobe might even come close to the top of the PHY domain restricting the movement of the entire HK domain. We anticipate that the restrained mobility of the HK domain reduces the overall heterogeneity of the HK domain with the Pr/Pfr heterodimer resulting in a better cryo-EM map than in either of the homodimers in this region. Once the kink is formed, further relaxations of the PCM may facilitate the Pr to Pfr transition of subunit A upon absorption of a second photon. This results in the described structural change of the sensory tongue and other structural changes also in subunit A (Fig. 3C and Fig. 5C,F,I). These structural changes then cause an additional kink in the linker helix of subunit B (Fig. 5F). We believe that the two kinks, one in the linker helix of subunit A, the other in that of subunit B, are structurally important for the rotation of the HK (Fig. 6C).

The HK rotation might open or exclude a binding site for a downstream RR. The X-ray structure of an unrelated RR/HK complex (PDB code: 3DGE) shows that the RR interacts mainly with the 4-helix bundle of the HK (*39*). The analog region in the SaBphP2 HK is shown in Fig. 3B (dashed box). Any structural change of the 4-helix bundle must have an immediate effect on the binding properties of the RR. Therefore, the rotation observed in the HK of SaBphP2 (movie S1) can have a fundamental influence on the binding, phosphorylation and dissociation, and consequently on the activation, of the RR. We anticipate that a sequence of similar events in the reverse photoreaction from the Pfr to the Pr state might be necessary to drive the BphP to the Pr state much faster than the slow dark reversion process shown in Fig. 2A.

Upon absorption of a photon, structural changes do not propagate simultaneously and symmetrically through both subunits within the protein dimer. One of the linker helices connecting the PCM to HK develops a kink first, the second kink can only form once a second photon is

absorbed. The kink forms near Phe485 (fig. S6C and D). Aromatic residues, especially phenylalanine, are known to have a high propensity for helical disruption (*40, 41*). Several studies have also reported asymmetric kink formation in the interface helices in the BphP of the plant pathogen *Xanthomonas campestris* (*21, 42*) (with an effector domain different from a HK) and also in other, unrelated sensory HKs (*43, 44*) where the kinks are associated with signal transduction and modulation (*43, 44*). In SaBphP2 the change in the hydration environment caused by exposure of the Phe485 hydrophobic sidechain to the polar solvent (fig. S6C,D) could break the hydrogen bonds that are stabilizing the linker helix (*21*). However, the helix could also be destabilized by the β-sheet to α-helix transition of the sensory tongue in one subunit that causes substantial structural relaxations along the dimer interface (compare Fig. 5G with 5H), which is also suggested for homologous BphPs (*45, 46*). The formation of the second kink after absorption of second photon might be the decisive structural reason for the subsequent rotation of the HK.

In crystal structures of the truncated DrBphP PCM (lacking the OM) which were determined in the Pfr state, the dimer interface of the PHY domains separate by up to ~30 Å (Fig. 7C) upon photoconversion (*25, 27*). However, the crystal structure of the bathy photochrome PCM from *P. aeruginosa* determined in the thermally stable Pfr state shows a parallel dimer interface (*33*). This agrees with the cryo-EM structures shown here of the homodimers in the Pfr state for both the truncated PCM and the full-length SaBphP2 (Fig. 7D). Notably, the cryo-EM structures of a DrBphP-RR chimera made by C-terminal fusion of RR to DrBphP did not show PHY domain separation in the Pfr state (*24*). This contrasts to the displacement of the PHY domains by ~14 Å in SaBphP2 (Fig. 4A,B) when comparing the Pr and Pfr states of the two homodimers (movie S1). The fusion of a RR protein to DrBphP may have hindered the necessary large-scale conformational changes as observed in our cryo-EM structures. On the other hand, the very large separation of the PHY domains in the crystal structures of the wild-type (*27*) and mutant (*25*) DrBphP PCMs may be induced by crystal contacts. Our cryo-EM structures of SaBphP2 in the Pfr state (in the full

length and truncated forms) are in agreement with Pr and Pfr structures of the full-length DrBphP captured by lower-resolution cryo-EM ten years ago (*46*). Despite ~27 Å resolution achieved in the earlier study, a ~35˚ rotation and a ~9 Å movement of the PHY domains has been determined (compared to ~30˚ and ~13 Å seen here). The rearrangement and rotation of individual domains within a single subunit of the SaBphP2 protein dimer are further supported by X-ray solution scattering studies (*47, 48*) and NMR investigations (*49*).

The majority of published phytochrome structures involve homodimers in parallel and antiparallel configurations, captured in the dark-adapted state (Pr for classical and Pfr for bathy phytochromes) (*15, 25-27*). A limited number of light-illuminated structures captured in the Pfr state show homodimers but involve modified proteins created by the deletion of the entire enzymatic domain (*27*), C-terminal fusions to stabilize full-length proteins (*24*) and/or mutations to slow down dark-reversion during crystallization (*25*). The only Pr/Pfr heterodimer structure was captured in the dark-adapted crystal form of the modified *Idiomarina* IsPadC that has a diguanylyl-cyclase activity (*50*) (Fig. 7A,B). Although the wild-type protein crystallized as a homodimer in the Pr state, the IsPadC crystallized as Pr/Pfr heterodimer under the same conditions when modified at several positions in the linker region. The two structures of IsPadC differ at the dimer interface. The overall tilt of the enzymatic domain in IsPadC heterodimer (Fig. 7A,B) further supports the role of asymmetric signaling in BphPs.

The SaBphP2 heterodimer structure revealed by cryo-EM with each subunit in distinct Pr and Pfr states shines light on the importance of asymmetric signaling in sensory kinases and that asymmetry can be induced already on the level of the PCM alone and is not dependent on modifications of the linker (as it is absent in the PCM). As such, our results point to the Pr/Pfr heterodimer as an intermediate in the photocycle. The sequence of photon absorptions by the individual subunits described above establishes an equilibrium between the homodimers in the Pr

297 and Pfr states that includes the Pr/Pfr heterodimer. The delicate balance between the three signaling
298 states of the Pr/Pfr photocycle can sensibly and quickly adapt to changes in light conditions to fine-
299 tune the HK activity. Specifically, the HK rotation and the adjustment of the HK structure,
300 subsequent interaction with the RR, its cross-phosphorylation, and its dissociation from the OM
301 can be adjusted to regulate red and far-red light dependent cellular responses of the myxobacteria.

302 In plant Phys such as the PhyB, the involvement of spectrally distinct Pr/Pfr heterodimers is
303 proposed (*51*) that help to fine-tune the spectral response in plant. Although we do not show a plant
304 Pr/Pfr heterodimer, we show with a BphP that phytochrome Pr/Pfr heterodimers exist since two
305 photons (one photon each by the two central chromophores) must be absorbed to transition from Pr
306 to Pfr or vice versa. In plants, long-range phytochrome signaling is likely to differ from BphPs.
307 Given multiple phytochrome genes in plants, phytochrome proteins are able to form heterodimers
308 composed of two different phytochrome proteins (*52*) which are integral for signaling (*53*). Since
309 *S. aurantiaca* has multiple BphPs (SaBphP1 and SaBphP2), P1/P2 heterodimers might also exist in
310 addition to Pr/Pfr heterodimers, in analogy to plants.

311 It would be desirable to determine the structure of the BphP in complex with a RR to gain
312 more insight in the function of two component systems. This will clarify where and to which of the
313 distinct signaling states of BphP, the RR binds. The conformational change of the sensory tongue
314 and the twisting of the PCM dimer interface helices during the Pr to Pfr transition are coupled.
315 Signal propagation via both the sensory tongue and the dimer interfaces is suggested but the
316 decisive conclusion is missing. Time-resolved (TR) cryo-EM presents a unique opportunity to study
317 these large-scale conformational changes. Initial successes with TR cryo-EM are reported (*54-56*).
318 The TR cryo-EM experiment will reveal the specific order of conformational changes that
319 ultimately trigger the enzymatic activity, and how the SaBphP2 dimers interact with the
320 downstream RR.

Material and Methods

Experimental Design. The intact SaBphP2 and its PCM were produced by overexpression in *E. coli* and purified. The purified phytochrome constructs were used (i) to obtain absorption spectra after exposure to various light conditions, (ii) to test the HK activity of the intact SaBphP2 using an autoradiography assay with ATP [γ-^{32}P] and (iii) to prepare sample grids under various light conditions that were rapidly frozen and imaged by cryo-EM.

Protein purification. The coding region of the wild-type SaBphP2 were PCR-amplified from *S. aurantiaca* DW4/3–1 genomic DNA and cut by restriction enzymes NdeI and HindIII (New England Biolabs, Beverly, USA), and ligated into the corresponding sites of the expression vector pET28c(+) (Invitrogen, Carlsbad, CA). The constructed plasmids and the pET11a vector carrying heme oxygenase were transformed into *Escherichia coli* BL21 (DE3) for expression. Cells were grown at 37° C to a OD_{600} value of 0.6 followed by induction with 1 mM IPTG and addition of 0.5 mM δ-aminolaevulinic acid (DAC) overnight. Cells were recovered in 150 mM NaCl, 20 mM Tris-HCl, pH 8.0 and 15% v/v glycerol with protease inhibitor. Lysis was performed with pulse sonication on ice bath. The insoluble cell debris was removed by highspeed centrifugation, and the supernatant was incubated with 200 μM BV in Dimethyl sulfoxide (DMSO) in the ratio 1:100 for 30 min at 4°C. The solution was applied to Talon Co^{+2} metal ion affinity chromatography column. The column was washed with high salt buffer (20 mM Tris-HCl, 1 M NaCl, pH 8.0) followed by low salt buffer (20 mM Tris-HCl, 50 mM NaCl, pH 8.0) with 20 column volumes each. The protein was eluted by 300 mM imidazole, 20 mM NaCl, 20 mM Tris-HCl, pH 8.0. After elution the protein was immediately transferred into stabilizing buffer containing 20 mM NaCl, 20 mM Tris-HCl, pH 8.0. Cells were grown in the dark, and all further steps were performed under dimmed white light. The purified protein was immediately frozen at -80° C and shipped on dry ice to the Simons Electron Microscopy Center (SEMC) of the New York Structural Biology Center (NYSBC) for cryo-EM experiments.

Absorption Spectra. Absorption spectra were recorded from solutions of ~ 0.4 mg/ml full length SaBphP2 (Fig. 2A) and the corresponding PCM construct (Fig. 2B). The solution was illuminated for 5 min with 740 nm light to prepare the Pr state (Fig. 2A,B, red lines) and with 660 nm light to shift the molecules to the Pfr state (Fig. 2A,B, dark red lines). After illumination with the respective wavelength, the solution was kept in the dark for 1 h and the spectra were retaken. The Pr spectra for both the full length SaBphP2 and the PCM did not change. The Pfr spectra slowly changed (arrows in Fig. 2A,B) towards to Pr spectra. The absorption spectra of the intact SaBphP2 and those of the PCM in the region between 500 nm and 840 nm are essentially identical and behave in a very similar way.

Histidine Kinase Test. To determine kinase activity, the three different species were prepared by keeping the SaBphP2 solution either at ambient white light or the solutions were illuminated for 5 min with 740 nm light or with 660 nm light to obtain pure Pr and Pfr species, respectively. Phosphorylation of SaBphP2 was conducted by mixing the SaBphP2 solutions with kinase buffer (20 mM Tris-HCl, pH 8.0, 50 mM KCl, 25 mM $MgCl_2$, and 1 μM PMSF) with 5 μCi of ATP [γ-^{32}P]. The mixtures of the pure species were illuminated for an additional 5 minutes with either 740 nm or 660 nm light to avoid backreactions and kept in the dark thereafter. All mixtures were incubated for 20 min after which the kinase reaction was terminated by adding 2 × sodium dodecyl sulfate (SDS) sample buffer. The samples were subject to SDS–polyacrylamide gel electrophoresis (PAGE) and stained with Coomassie blue. After the gel has been dehydrated, it was autoradiographed using a Typhoon Phosphorimager (GE Healthcare). Strong radioactivity appears at a position that overlays exactly with the Coomassie stained band in the gel (Fig. 2C). The SaBphP2 is a HK. To examine whether there is a difference between the HK activity of the Pr and Pfr form, we added 10 μM of cold ATP to the kinase buffer in addition to the ATP [γ-^{32}P]. 8 ul of a SaBphP2 solution was illuminated for 5 min with either 740 nm or 660 nm light to prepare the Pr and Pfr conformations, respectively, before the ATP containing kinase buffer was added.

Phosphorylation of SaBphP2 was conducted in the same way as described, except that the incubation time was much shorter between 1 and 8 minutes. Results shown in Fig. 2D demonstrate that the SaBphP2 is more active in the Pr state compared to the Pfr state.

Grid preparation for cryo-EM. UltrAuFoil holey grids (300 mesh R1.2/1.3, Quantifoil) were plasma-cleaned for 7 s using oxygen and argon gases with a Solarus II Gatan Plasma System. The grids were vitrified by plunging into liquid ethane on an FEI Vitrobot automatic plunge freezer with a blotting time of 1 seconds and incubation time of 10 seconds. To obtain the full-length SaBphP2 Pr/Pfr heterodimer, the protein was frozen at a concentration of 0.3 mg/mL in purification buffer (50 mM NaCl, 20 mM Tris-HCl, pH 8.0) with a blotting time of 1.5 seconds under standard laboratory fluorescent light conditions. No extra care was taken to prevent the photo reaction of the protein under ambient white light. To obtain SaBphP2 in the pure Pr and pure Pfr homodimeric states, sample grids were prepared under green safety light, at a concentration of 0.4 mg/mL. The pure Pr state was produced by pre-illumination with 740 nm light, while the pure Pfr state was obtained by pre-illumination with 660 nm light. Grids with the shorter PCM construct were also prepared at ambient white light. In addition, preparations of the PCM were pre-illuminated with 640 nm light to obtain a homogenous Pfr state. The concentration of the PCM was adjusted to 0.7 mg/ml. For all samples that required controlled irradiation, the illumination time was set to 5 minutes. The grids were immediately frozen to prevent any further reactions. All frozen grids were clipped in AutoGrid cartridges (Thermo Fisher Scientific) and stored in liquid nitrogen until data acquisition.

Data Acquisition. All grids were imaged on a Thermo Fisher Scientific Titan Krios microscope equipped with a Gatan BioQuantum K3 energy filter direct electron detector camera. Movies with SaBphP2 in the pure Pr state were collected in counting mode with a 2000 ms exposure time, 50 frames, 40 ms per frame and a total dose of 56.39 e-/Å2. A total of 15,533 movies were collected at a pixel size of 0.844 Å/px. Movies of SaBphP2 in the pure Pfr state were collected in counting

mode with a 2000 ms exposure time, 50 frames, 40 ms per frame and a total dose of 59.31 e-/Å2. A total of 19,607 movies were collected at a pixel size of 0.844 Å/px. Movies of the SaBphP2 Pr/Pfr heterodimer were collected in counting mode with a 2000 ms exposure time, 50 frames, 40 ms per frame and a total dose of 67.02 e-/Å2. A total of 17,880 movies were collected at a pixel size of 0.844 Å/px. Movies on the (shorter) PCM in the all-Pfr state were collected in counting mode with a 2000 ms exposure time, 50 frames, 40 ms per frame and a total dose of 49.78 e-/Å2. A total of 19,607 movies were collected at a pixel size of 0.844 Å/px. Movies on the PCM in the heterodimeric state were collected with a 2000 ms exposure time, 50 frames, 40ms per frame and a total dose of 49.78 e-/Å2. A total of 17,707 movies were collected with a super-resolution pixel size of 0.422 Å/px. All data acquisition was done using Leginon (*57*). Details for data analysis and structure determination are provided in the supplementary material.

References

1. A. M. Stock, V. L. Robinson, P. N. Goudreau, Two-component signal transduction. *Annu Rev Biochem* **69**, 183-215 (2000).
2. M. Furuya, Phytochromes: their molecular species, gene families, and functions. *Annu. Rev. Plant Physiol.* **44**, 617 - 645 (1993).
3. N. C. Rockwell, Y. S. Su, J. C. Lagarias, Phytochrome structure and signaling mechanisms. *Annual review of plant biology* **57**, 837-858 (2006).
4. S. J. Davis, A. V. Vener, R. D. Vierstra, Bacteriophytochromes: Phytochrome-like photoreceptors from nonphotosynthetic eubacteria. *Science* **286**, 2517-2520 (1999).
5. H. Li, E. S. Burgie, Z. T. K. Gannam, H. Li, R. D. Vierstra, Plant phytochrome B is an asymmetric dimer with unique signalling potential. *Nature* **604**, 127-133 (2022).
6. Y. Zhang, X. Lin, C. Ma, J. Zhao, X. Shang, Z. Wang, B. Xu, N. Gao, X. W. Deng, J. Wang, Structural insights into plant phytochrome A as a highly sensitized photoreceptor. *Cell Res* **33**, 806-809 (2023).
7. A. Batschauer, Photoreceptors of higher plants. *Planta* **206**, 479-492 (1998).
8. M. C. Cheng, P. K. Kathare, I. Paik, E. Huq, Phytochrome Signaling Networks. *Annual review of plant biology* **72**, 217-244 (2021).
9. K. Evans, A. P. Fordham-Skelton, H. Mistry, C. D. Reynolds, A. M. Lawless, M. Z. Papiz, A bacteriophytochrome regulates the synthesis of LH4 complexes in Rhodopseudomonas palustris. *Photosynth Res* **85**, 169-180 (2005).
10. N. C. Rockwell, L. Shang, S. S. Martin, J. C. Lagarias, Distinct classes of red/far-red photochemistry within the phytochrome superfamily. *Proceedings of the National Academy of Sciences of the United States of America* **106**, 6123-6127 (2009).
11. T. Lamparter, P. Xue, A. Elkurdi, G. Kaeser, L. Sauthof, P. Scheerer, N. Krauss, Phytochromes in Agrobacterium fabrum. *Front Plant Sci* **12**, 642801 (2021).

12. J. R. Wagner, J. S. Brunzelle, K. T. Forest, R. D. Vierstra, A light-sensing knot revealed by the structure of the chromophore-binding domain of phytochrome. *Nature* **438**, 325-331 (2005).
13. N. C. Woitowich, A. S. Halavaty, P. Waltz, C. Kupitz, J. Valera, G. Tracy, K. D. Gallagher, E. Claesson, T. Nakane, S. Pandey, G. Nelson, R. Tanaka, E. Nango, E. Mizohata, S. Owada, K. Tono, Y. Joti, A. C. Nugent, H. Patel, A. Mapara, J. Hopkins, P. Duong, D. Bizhga, S. E. Kovaleva, R. St Peter, C. N. Hernandez, W. B. Ozarowski, S. Roy-Chowdhuri, J. H. Yang, P. Edlund, H. Takala, J. Ihalainen, J. Brayshaw, T. Norwood, I. Poudyal, P. Fromme, J. C. H. Spence, K. Moffat, S. Westenhoff, M. Schmidt, E. A. Stojkovic, Structural basis for light control of cell development revealed by crystal structures of a myxobacterial phytochrome. *IUCrJ* **5**, 619-634 (2018).
14. M. E. Auldridge, K. T. Forest, Bacterial phytochromes: More than meets the light. *Crit Rev Biochem Mol* **46**, 67-88 (2011).
15. J. C. Sanchez, M. Carrillo, S. Pandey, M. Noda, L. Aldama, D. Feliz, E. Claesson, W. Y. Wahlgren, G. Tracy, P. Duong, A. C. Nugent, A. Field, V. Srajer, C. Kupitz, S. Iwata, E. Nango, R. Tanaka, T. Tanaka, L. Fangjia, K. Tono, S. Owada, S. Westenhoff, M. Schmidt, E. A. Stojkovic, High-resolution crystal structures of amyxobacterial phytochrome at cryo and roomtemperatures. *Struct Dyn* **6**, 054701 (2019).
16. G. T. Qualls, K. Stephens, D. White, Light-stimulated morphogenesis in the fruiting myxobacterium Stigmatella aurantiaca. *Science* **201**, 444-445 (1978).
17. D. White, W. Shropshire, Jr., K. Stephens, Photocontrol of development by Stigmatella aurantiaca. *J Bacteriol* **142**, 1023-1024 (1980).
18. T. F. Schaberle, F. Lohr, A. Schmitz, G. M. Konig, Antibiotics from myxobacteria. *Nat Prod Rep* **31**, 953-972 (2014).
19. P. Lapuhs, E. Heinrich, R. Garcia, A. Goes, N. Frank, L. Bollenbach, V. Stibane, T. Kuhn, M. Koch, A. K. Kiemer, R. Muller, K. Fuhrmann, G. Fuhrmann, The inherent antibiotic activity of myxobacteria-derived autofluorescent outer membrane vesicles is switched on and off by light stimulation. *Nanoscale* **14**, 17534-17542 (2022).
20. M. Kojadinovic, A. Laugraud, L. Vuillet, J. Fardoux, L. Hannibal, J. M. Adriano, P. Bouyer, E. Giraud, A. Vermeglio, Dual role for a bacteriophytochrome in the bioenergetic control of Rhodopseudomonas palustris: enhancement of photosystem synthesis and limitation of respiration. *Biochimica et biophysica acta* **1777**, 163-172 (2008).
21. L. H. Otero, S. Klinke, J. Rinaldi, F. Velazquez-Escobar, M. A. Mroginski, M. Fernandez Lopez, F. Malamud, A. A. Vojnov, P. Hildebrandt, F. A. Goldbaum, H. R. Bonomi, Structure of the Full-Length Bacteriophytochrome from the Plant Pathogen Xanthomonas campestris Provides Clues to its Long-Range Signaling Mechanism. *Journal of molecular biology* **428**, 3702-3720 (2016).
22. E. Giraud, S. Zappa, L. Vuillet, J. M. Adriano, L. Hannibal, J. Fardoux, C. Berthomieu, P. Bouyer, D. Pignol, A. Vermeglio, A new type of bacteriophytochrome acts in tandem with a classical bacteriophytochrome to control the antennae synthesis in Rhodopseudomonas palustris. *Journal of Biological Chemistry* **280**, 32389-32397 (2005).
23. G. Gourinchas, S. Etzl, C. Gobl, U. Vide, T. Madl, A. Winkler, Long-range allosteric signaling in red light-regulated diguanylyl cyclases. *Sci Adv* **3**, e1602498 (2017).
24. W. Y. Wahlgren, E. Claesson, I. Tuure, S. Trillo-Muyo, S. Bodizs, J. A. Ihalainen, H. Takala, S. Westenhoff, Structural mechanism of signal transduction in a phytochrome histidine kinase. *Nat Commun* **13**, 7673 (2022).
25. E. S. Burgie, J. Zhang, R. D. Vierstra, Crystal Structure of Deinococcus Phytochrome in the Photoactivated State Reveals a Cascade of Structural Rearrangements during Photoconversion. *Structure* **24**, 448-457 (2016).

26. M. Carrillo, S. Pandey, J. Sanchez, M. Noda, I. Poudyal, L. Aldama, T. N. Malla, E. Claesson, W. Y. Wahlgren, D. Feliz, V. Srajer, M. Maj, L. Castillon, S. Iwata, E. Nango, R. Tanaka, T. Tanaka, L. Fangjia, K. Tono, S. Owada, S. Westenhoff, E. A. Stojkovic, M. Schmidt, High-resolution crystal structures of transient intermediates in the phytochrome photocycle. *Structure* **29**, 743-754 (2021).
27. H. Takala, A. Bjorling, O. Berntsson, H. Lehtivuori, S. Niebling, M. Hoernke, I. Kosheleva, R. Henning, A. Menzel, J. A. Ihalainen, S. Westenhoff, Signal amplification and transduction in phytochrome photosensors. *Nature* **509**, 245-248 (2014).
28. M. F. Lopez, M. Dahl, F. V. Escobar, H. R. Bonomi, A. Kraskov, N. Michael, M. A. Mroginski, P. Scheerer, P. Hildebrandt, Photoinduced reaction mechanisms in prototypical and bathy phytochromes. *Physical chemistry chemical physics : PCCP* **24**, 11967-11978 (2022).
29. A. Bjorling, O. Berntsson, H. Takala, K. D. Gallagher, H. Patel, E. Gustavsson, R. St Peter, P. Duong, A. Nugent, F. Zhang, P. Berntsen, R. Appio, I. Rajkovic, H. Lehtivuori, M. R. Panman, M. Hoernke, S. Niebling, R. Harimoorthy, T. Lamparter, E. A. Stojkovic, J. A. Ihalainen, S. Westenhoff, Ubiquitous Structural Signaling in Bacterial Phytochromes. *The journal of physical chemistry letters* **6**, 3379-3383 (2015).
30. L. O. Essen, J. Mailliet, J. Hughes, The structure of a complete phytochrome sensory module in the Pr ground state. *Proceedings of the National Academy of Sciences of the United States of America* **105**, 14709-14714 (2008).
31. E. A. Stojkovic, K. C. Toh, M. T. Alexandre, M. Baclayon, K. Moffat, J. T. Kennis, FTIR Spectroscopy Revealing Light-Dependent Refolding of the Conserved Tongue Region of Bacteriophytochrome. *The journal of physical chemistry letters* **5**, 2512-2515 (2014).
32. X. Yang, E. A. Stojkovic, J. Kuk, K. Moffat, Crystal structure of the chromophore binding domain of an unusual bacteriophytochrome, RpBphP3, reveals residues that modulate photoconversion. *Proceedings of the National Academy of Sciences of the United States of America* **104**, 12571-12576 (2007).
33. X. Yang, J. Kuk, K. Moffat, Crystal structure of Pseudomonas aeruginosa bacteriophytochrome: photoconversion and signal transduction. *Proceedings of the National Academy of Sciences of the United States of America* **105**, 14715-14720 (2008).
34. E. S. Burgie, A. N. Bussell, J. M. Walker, K. Dubiel, R. D. Vierstra, Crystal structure of the photosensing module from a red/far-red light-absorbing plant phytochrome. *Proceedings of the National Academy of Sciences of the United States of America* **111**, 10179-10184 (2014).
35. Q. H. Tran, O. M. Eder, A. Winkler, Dynamics-driven allosteric stimulation of diguanylate cyclase activity in a red light regulated phytochrome. *The Journal of biological chemistry* **300**, 107217 (2024).
36. P. Edlund, H. Takala, E. Claesson, L. Henry, R. Dods, H. Lehtivuori, M. Panman, K. Pande, T. White, T. Nakane, O. Berntsson, E. Gustavsson, P. Bath, V. Modi, S. Roy-Chowdhury, J. Zook, P. Berntsen, S. Pandey, I. Poudyal, J. Tenboer, C. Kupitz, A. Barty, P. Fromme, J. D. Koralek, T. Tanaka, J. Spence, M. Liang, M. S. Hunter, S. Boutet, E. Nango, K. Moffat, G. Groenhof, J. Ihalainen, E. A. Stojkovic, M. Schmidt, S. Westenhoff, The room temperature crystal structure of a bacterial phytochrome determined by serial femtosecond crystallography. *Scientific reports* **6**, 35279 (2016).
37. A. Marina, C. D. Waldburger, W. A. Hendrickson, Structure of the entire cytoplasmic portion of a sensor histidine-kinase protein. *The EMBO journal* **24**, 4247-4259 (2005).
38. A. Punjani, J. L. Rubinstein, D. J. Fleet, M. A. Brubaker, cryoSPARC: algorithms for rapid unsupervised cryo-EM structure determination. *Nature methods* **14**, 290-296 (2017).
39. P. Casino, V. Rubio, A. Marina, Structural Insight into Partner Specificity and Phosphoryl Transfer in Two-Component Signal Transduction. *Cell* **139**, 325-336 (2009).

40. Y. H. Huang, C. M. Chen, Statistical analyses and computational prediction of helical kinks in membrane proteins. *Journal of computer-aided molecular design* **26**, 1171-1185 (2012).
41. H. R. Wilman, J. Shi, C. M. Deane, Helix kinks are equally prevalent in soluble and membrane proteins. *Proteins* **82**, 1960-1970 (2014).
42. L. H. Otero, S. Foscaldi, G. T. Antelo, G. L. Rosano, S. Sirigu, S. Klinke, L. A. Defelipe, M. Sanchez-Lamas, G. Battocchio, V. Conforte, A. A. Vojnov, L. M. G. Chavas, F. A. Goldbaum, M. A. Mroginski, J. Rinaldi, H. R. Bonomi, Structural basis for the Pr-Pfr long-range signaling mechanism of a full-length bacterial phytochrome at the atomic level. *Sci Adv* **7**, eabh1097 (2021).
43. R. P. Diensthuber, M. Bommer, T. Gleichmann, A. Moglich, Full-length structure of a sensor histidine kinase pinpoints coaxial coiled coils as signal transducers and modulators. *Structure* **21**, 1127-1136 (2013).
44. H. U. Ferris, M. Coles, A. N. Lupas, M. D. Hartmann, Crystallographic snapshot of the Escherichia coli EnvZ histidine kinase in an active conformation. *Journal of structural biology* **186**, 376-379 (2014).
45. X. Yang, E. A. Stojkovic, W. B. Ozarowski, J. Kuk, E. Davydova, K. Moffat, Light Signaling Mechanism of Two Tandem Bacteriophytochromes. *Structure* **23**, 1179-1189 (2015).
46. E. S. Burgie, T. Wang, A. N. Bussell, J. M. Walker, H. Li, R. D. Vierstra, Crystallographic and electron microscopic analyses of a bacterial phytochrome reveal local and global rearrangements during photoconversion. *The Journal of biological chemistry* **289**, 24573-24587 (2014).
47. A. Bjorling, O. Berntsson, H. Lehtivuori, H. Takala, A. J. Hughes, M. Panman, M. Hoernke, S. Niebling, L. Henry, R. Henning, I. Kosheleva, V. Chukharev, N. V. Tkachenko, A. Menzel, G. Newby, D. Khakhulin, M. Wulff, J. A. Ihalainen, S. Westenhoff, Structural photoactivation of a full-length bacterial phytochrome. *Sci Adv* **2**, e1600920 (2016).
48. H. Takala, S. Niebling, O. Berntsson, A. Bjorling, H. Lehtivuori, H. Hakkanen, M. Panman, E. Gustavsson, M. Hoernke, G. Newby, F. Zontone, M. Wulff, A. Menzel, J. A. Ihalainen, S. Westenhoff, Light-induced structural changes in a monomeric bacteriophytochrome. *Struct Dyn* **3**, 054701 (2016).
49. L. Isaksson, E. Gustavsson, C. Persson, U. Brath, L. Vrhovac, G. Karlsson, V. Orekhov, S. Westenhoff, Signaling Mechanism of Phytochromes in Solution. *Structure*, (2020).
50. G. Gourinchas, U. Heintz, A. Winkler, Asymmetric activation mechanism of a homodimeric red light-regulated photoreceptor. *eLife* **7**, 34815 (2018).
51. C. Klose, F. Venezia, A. Hussong, S. Kircher, E. Schafer, C. Fleck, Systematic analysis of how phytochrome B dimerization determines its specificity. *Nat Plants* **1**, 15090 (2015).
52. T. Clack, A. Shokry, M. Moffet, P. Liu, M. Faul, R. A. Sharrock, Obligate heterodimerization of Arabidopsis phytochromes C and E and interaction with the PIF3 basic helix-loop-helix transcription factor. *Plant Cell* **21**, 786-799 (2009).
53. R. A. Sharrock, T. Clack, Heterodimerization of type II phytochromes in. *Proceedings of the National Academy of Sciences of the United States of America* **101**, 11500-11505 (2004).
54. V. P. Dandey, W. C. Budell, H. Wei, D. Bobe, K. Maruthi, M. Kopylov, E. T. Eng, P. A. Kahn, J. E. Hinshaw, N. Kundu, C. M. Nimigean, C. Fan, N. Sukomon, S. A. Darst, R. M. Saecker, J. Chen, B. Malone, C. S. Potter, B. Carragher, Time-resolved cryo-EM using Spotiton. *Nature methods* **17**, 897-900 (2020).

55. S. Torino, M. Dhurandhar, A. Stroobants, R. Claessens, R. G. Efremov, Time-resolved cryo-EM using a combination of droplet microfluidics with on-demand jetting. *Nature methods* **20**, 1400-1408 (2023).
56. J. Frank, Time-resolved cryo-electron microscopy: Recent progress. *Journal of structural biology* **200**, 303-306 (2017).
57. C. Suloway, J. Pulokas, D. Fellmann, A. Cheng, F. Guerra, J. Quispe, S. Stagg, C. S. Potter, B. Carragher, Automated molecular microscopy: the new Leginon system. *Journal of structural biology* **151**, 41-60 (2005).

58. P. Emsley, B. Lohkamp, W. G. Scott, K. Cowtan, Features and development of Coot. *Acta crystallographica. Section D, Biological crystallography* **66**, 486-501 (2010).
59. E. F. Pettersen *et al.*, UCSF ChimeraX: Structure visualization for researchers, educators, and developers. *Protein Sci* **30**, 70-82 (2021).
60. D. Liebschner *et al.*, Macromolecular structure determination using X-rays, neutrons and electrons: recent developments in Phenix. *Acta Crystallogr D Struct Biol* **75**, 861-877 (2019).
61. J. Jumper *et al.*, Highly accurate protein structure prediction with AlphaFold. *Nature* **596**, 583-589 (2021).

Acknowledgements:

We thank Madhusudan (Madhu) Dey, UWM Biology Department, for help with the ATP [^{32}P] assay.

Funding:

National Science Foundation NSF-STC-1231306 BioXFEL (MS, PS)

National Science Foundation BioXFEL center award 6227 (ES)

National Institute of General Medical Sciences (NIGMS) Maximizing Access to Research Careers (MARC)-T34 GM105549 grant (ES)

Simons Foundation grant SF349247 (CH, JHM)

National Institute of General Medical Sciences, grant GM103310 (CH, JHM)

Support by NYSTAR and the New York State Assembly Majority (CH, JHM)

Author contributions:

Conceptualization: TNM, EAS, MS

Sample Preparation: DM, DB, SM, TNM

Methodology: TNM, CH, JHM, SM, PS, MS

Data collection: CH, JHM, SM

Data analysis: TNM, CH, JHM

Visualization: TNM, MS

Funding acquisition: EAS, MS, JHM

Project administration: TNM, EAS, MS

Supervision: EAS, MS

Writing the original draft: TNM, EAS, MS with input from all authors.

Competing interest: The authors declare that they have no competing interests.

Data and materials availability: All data needed to evaluate the conclusions in the paper are present in the paper and/or the Supplementary Materials. Cryo-EM maps and atomic models were deposited to the Electron Microscopy Data Bank (EMDB) and Protein Data Bank (PDB) databases. The PDB codes are: 8UPH (full-length Pr state), 8UPM (full-length Pfr state), 8UPK (full-length hybrid state), 8UQK (PCM Pfr state) and 8UQI (PCM hybrid state). The EMDB accession codes are EMD-42448 (full-length Pr state), EMD-42452 (full-length Pfr state), EMD-42450 (full-length hybrid state), EMD-42469 (PCM Pfr state) and EMD-42472 (PCM hybrid state). Atomic coordinates of other phytochromes used for comparison in this study are available in the PDB under accession codes 6ET7, 3G6O and 4O01 respectively.

Table of contents for the supplementary material:

Supplementary Methods and Results

Figs. S1 to S6

Table S1

Movie S1

References 58 to 61

Figures:

Figure 1

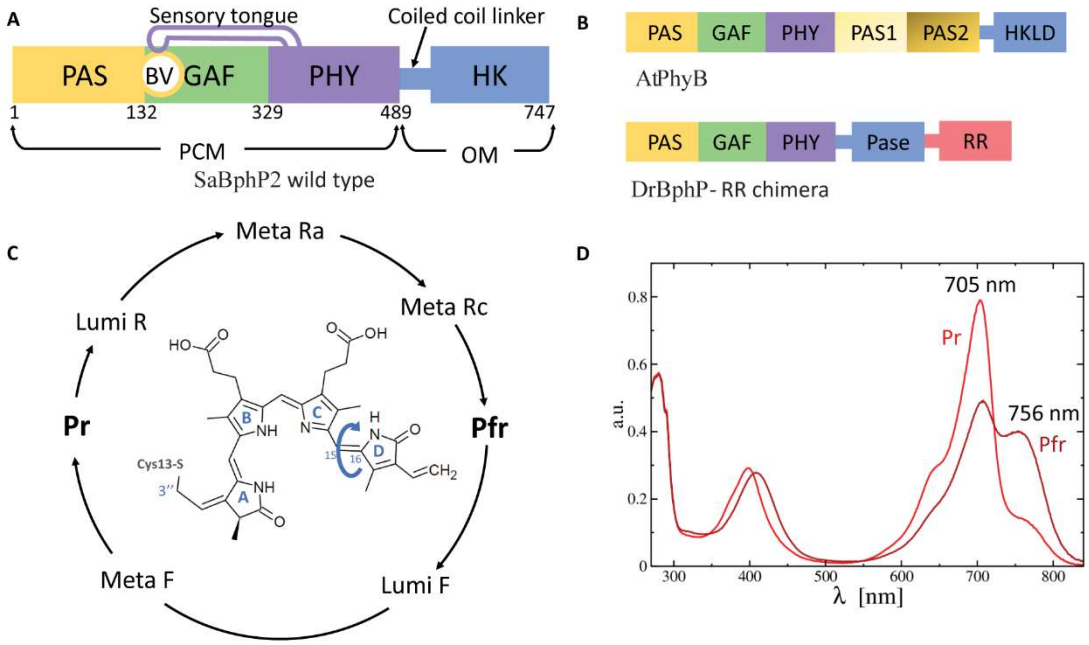

649

Figure 2

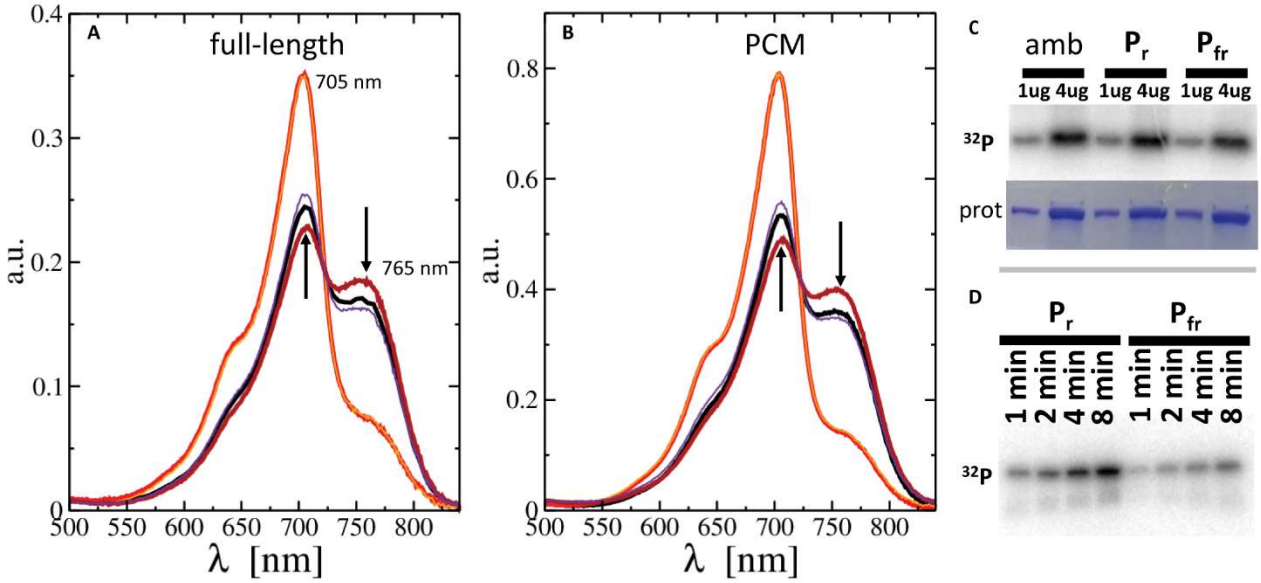

650

651

652

653

654 **Figure 3**

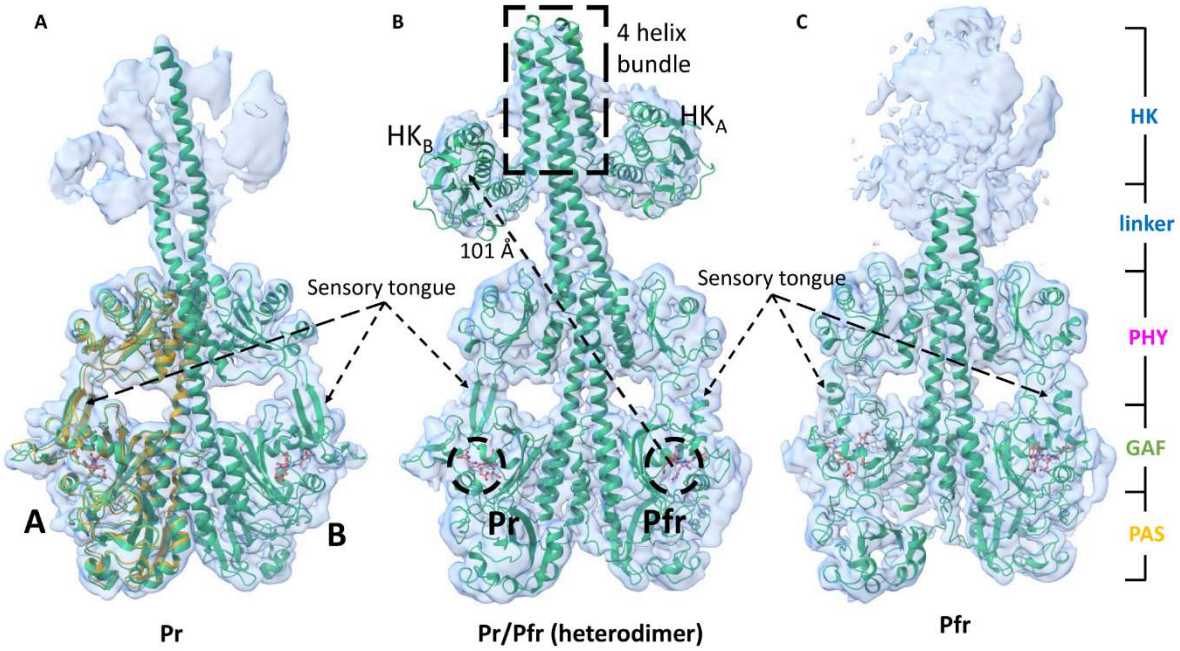

655

656

657

658

Figure 4

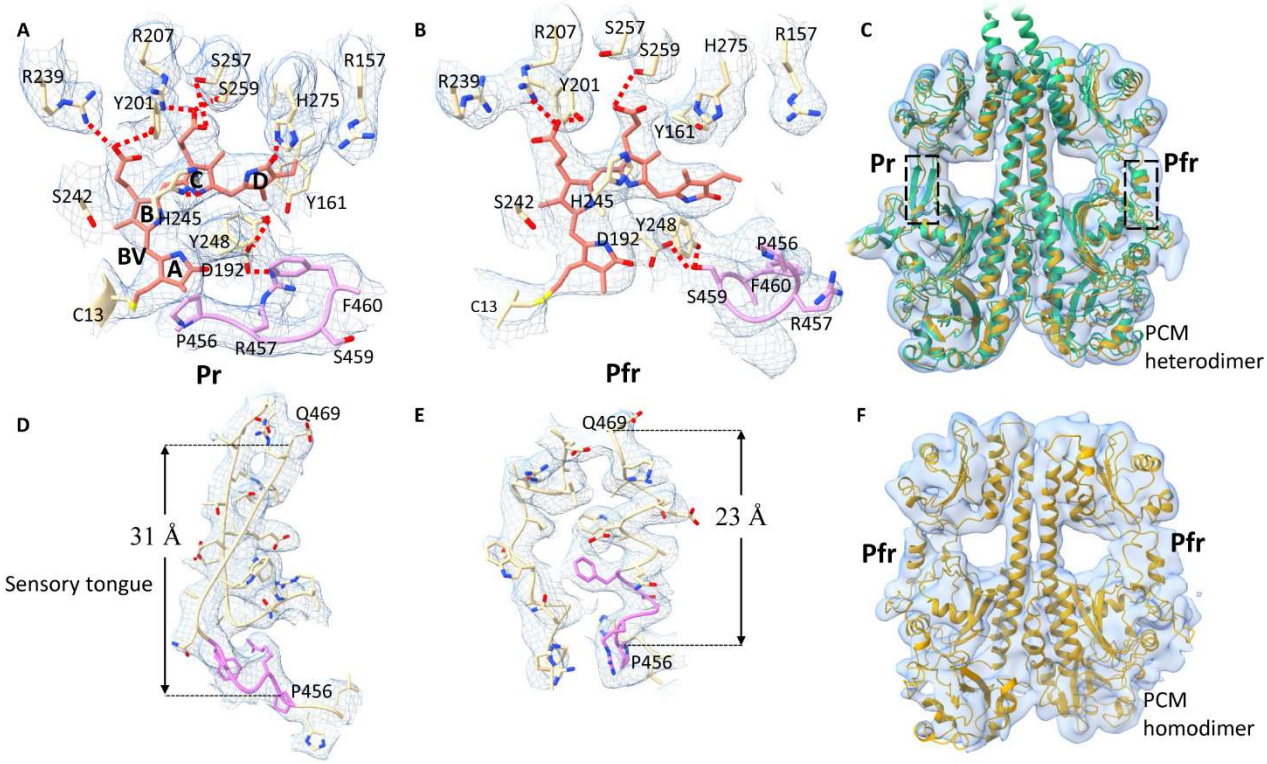
A
R207
S257
R157
R239
S259
Y201
H275
S242
C
D
Y161
B
H245
Y248
BV
A
D192
C13
F460
P456
R457
S459
Pr
B
R207
S257
S259
H275
R157
R239
Y201
Y161
S242
H245
Y248
D192
P456
F460
S459
C13
R457
Pfr
C
Pr
Pfr
PCM
heterodimer
D
Q469
31 Å
Sensory tongue
P456
E
Q469
23 Å
P456
F
Pfr
Pfr
PCM
homodimer

Figure 5

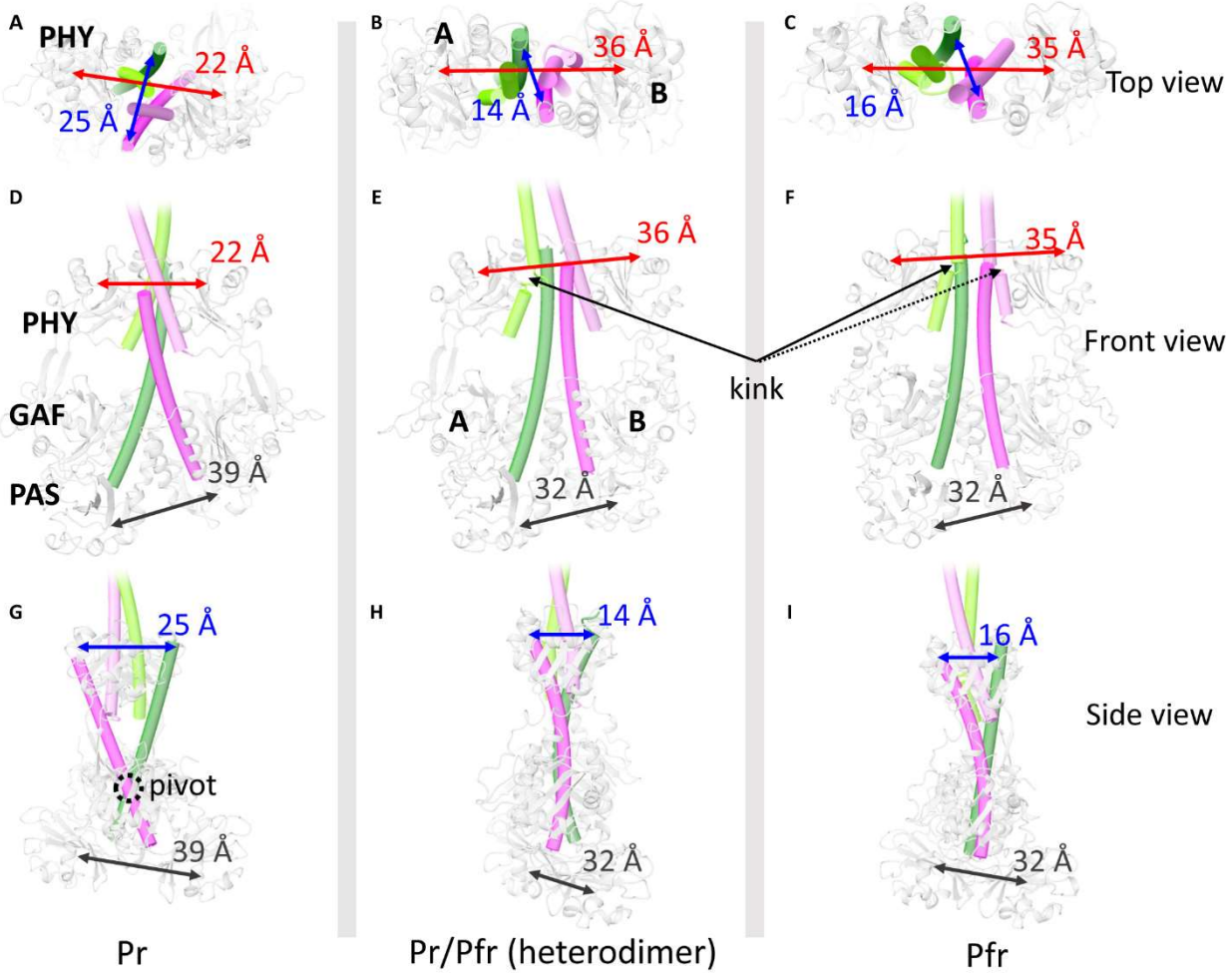
A
PHY
22 Å
25 Å
B
A
36 Å
14 Å
B
C
35 Å
16 Å
Top view
D
22 Å
PHY
GAF
PAS
39 Å
E
36 Å
A
B
32 Å
kink
F
35 Å
32 Å
Front view
G
25 Å
pivot
39 Å
H
14 Å
32 Å
I
16 Å
32 Å
Side view
Pr
Pr/Pfr (heterodimer)
Pfr

Figure 6

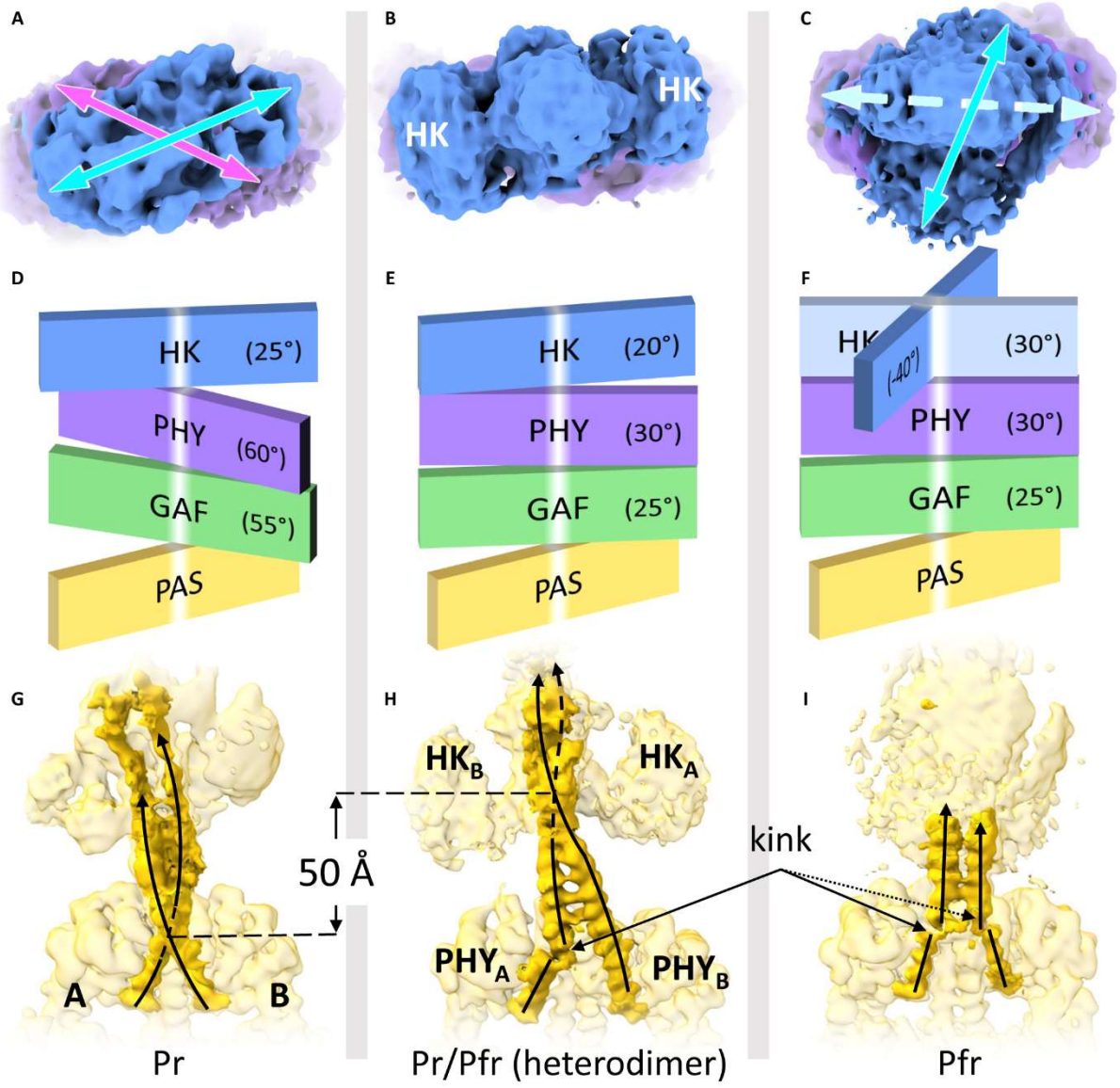
A
B
HK
HK
C
D
HK (25°)
PHY (60°)
GAF (55°)
PAS
E
HK (20°)
PHY (30°)
GAF (25°)
PAS
F
HK
(-40°)
(30°)
PHY (30°)
GAF (25°)
PAS
G
A
B
50 Å
H
HK$_B$
HK$_A$
PHY$_A$
PHY$_B$
I
kink
Pr
Pr/Pfr (heterodimer)
Pfr

Figure 7

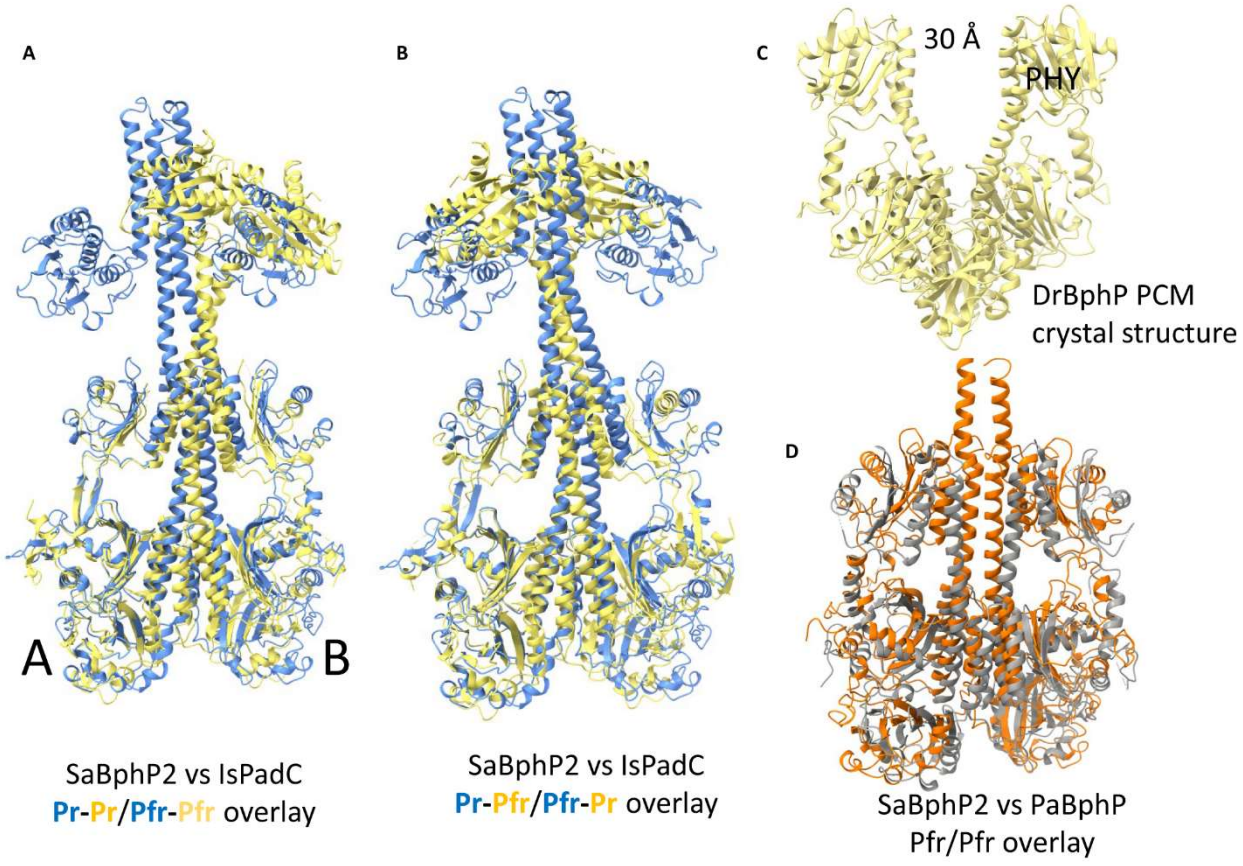
A
B
C
30 Å
PHY
DrBphP PCM
crystal structure
D
A
B
SaBphP2 vs IsPadC
Pr-Pr/Pfr-Pfr overlay
SaBphP2 vs IsPadC
Pr-Pfr/Pfr-Pr overlay
SaBphP2 vs PaBphP
Pfr/Pfr overlay

673 **Figure Captions:**

674

675 **Figure 1. *S. aurantiaca* BphP2 domain composition and Pr/Pfr photocycle.** (**A**) Domain
676 architecture of the wildtype SaBphP2. Amino acid sequence numbers are marked for each domain.
677 The BV chromophore is bound to a conserved cysteine (Cys13). The BV binding pocket is located
678 within the GAF domain. The sensory tongue as an extension of the PHY domain (purple) is
679 highlighted. (**B**) Domain compositions of the *A. thaliana* plant PhyB and the *D. radiodurans* BphP-
680 RR chimera. The AtPhyB features additional PAS domains and a histidine kinase like domain
681 (HKLD). The DrBphP's effector domain has phosphatase (Pase) activity. (**C**) The Pr/Pfr reversible
682 photocycle of SaBphP2. The structure of BV is shown with the 4 pyrrole rings (A – D). The rotation
683 of pyrrole ring D about the C_{15}=C_{16} double bond changes its configuration from *Z* to *E* (the
684 isomerization is shown by a blue arrow). (**D**) Absorption spectra of the SaBphP2-PCM with red
685 (705 nm) and far-red (756 nm) absorbing Pr (highlighted in red) and Pfr (highlighted in dark red)
686 states, respectively.

687

688 **Figure 2**. **Absorption spectra and HK activity of SaBphP2.** Spectra of the full length (**A**) and
689 the PCM (**B**) from 500 nm to 850 nm, obtained after exposure to ambient white light (black),
690 illumination by 660 nm light (red) and 740 nm light (dark-red). Spectra obtained after 1 hr in the
691 dark following 660 nm illumination are shown in purple (arrows denote the directions of the spectral
692 changes), those following after 740 nm illumination are shown in orange (spectra shown by red and
693 orange lines are identical). Absorption maxima are indicated in (**A**) and are essentially identical in
694 (**B**). Autophosphorylation of SaBphP2 with ATP [γ-^{32}P] (**C**) under ambient white light (amb), 740
695 nm (Pr state) and 660 nm (Pfr state) illumination and incubation for 20 min; the Coomassie stained
696 (prot) gel is shown below. (**D**) 740 nm (Pr state) and 660 nm (Pfr state) illumination and incubation
697 for 1 min to 8 min.

Figure 3. The cryo-EM–structures of full-length SaBphP2 dimer. The protein structures are shown by green ribbons with corresponding maps displayed in light blue. (**A**) In the homodimer of the Pr state, the sensory tongue of the PHY domain in each subunit is in the β-sheet conformation. One of the subunits in the crystal structure of the SaBphP2 PCM (PDB code: 6PTQ), determined in the Pr state, is overlaid (orange ribbons) on subunit A. (**B**) In the Pr/Pfr heterodimer, the configuration of the sensory tongue is an α-helix in one subunit and a β-strand in the other. The linker crosses subunit boundaries so that the lobe of the HK in subunit A is placed on the side of subunit B and vice-versa. The HK lobes are marked as HK_B and HK_A. The 4-helix bundle is marked by a dashed box, the locations of the BV chromophores by dashed circles. The distance between the BV chromophore and the center of the corresponding HK lobe is marked. (**C**) In the subunits of the Pfr state, both sensory tongues are in the α-helix conformation. The approximate domain locations within the full-length protein are marked on the right.

Figure 4. Pr/Pfr photoconversion in SaBphP2. (**A**) BV binding pocket in the Pr state. The BV (orange) ring D is in the *Z*-configuration. Amino acid side chains located in the GAF domain are marked in yellow and those in the PRXSF motif are shown in pink. Hydrogen bonds are marked by red dotted lines. (**B**) BV binding pocket in SaBphP2 in the Pfr state. The BV (orange) ring D is in the *E*-configuration. Nearby amino acid residues are marked. Hydrogen bonds are shown by red dotted lines. (**C**) The Pr/Pfr heterodimer of the PCM (gold color) is overlayed with the corresponding structure of the full-length SaBphP2 Pr/Pfr heterodimer (green). The two PCM structures are essentially identical. The regions within the dashed boxes are enlarged in (**D**) and (**E**). (**D**) The sensory tongue forms two β-strands in the Pr state. (**E**) In the Pfr state, the strand containing the PRXSF motif changes to an α-helix with Pro456 at the beginning. The changes in the length of the sensory tongues (in Å) are depicted in (**D**) and (**E**). (**F**) The homodimer of the SaBphP2 PCM in the Pfr state. The structure is shown in gold color. Cryo-EM maps are shown in light blue in all panels.

Figure 5. The dimer interface of the intact SaBphP2. Top (**A**, **B**, **C**), front (**D**, **E**, **F**) and side (**G**, **H**, **I**) views for the 3 cryo-EM structures. The helices at the dimer interface are colored in green (subunit A) and pink (subunit B) to differentiate individual subunits as marked in (**A**) and (**D**) with the ribbon diagram of the PCM shown in gray. The two linker helices are shown in light green (subunit A) and light pink (subunit B). Arrows indicate the distances between PAS domains (black, between corresponding Pro89 c_{α}-atoms), the PHY domains (red, between corresponding Gly358 c_{α}-atoms) and those of the dimer interface helices near the top of the PCM (blue). Distances are measured in Å. The pivot point about which the two subunits rotate is shown in (**G**) as a dotted circle. The kink in the coiled coil linker connecting the PCM and the HK in subunit A of the Pr/Pfr heterodimer (with subunit A in the Pr and subunit B in the Pfr state) is marked in (**E**). Both kinks that are apparent in the homodimer in the Pfr state are marked in (**F**).

Figure 6. Domain rearrangements within the SaBphP2. Top view of the cryo-EM maps of the HK domain in the Pr homodimer (**A**), Pr/Pfr heterodimer (**B**) and Pfr homodimer (**C**). In (**A**) the arrows indicate the orientations of the PHY (purple) and HK (blue) domains. In (**C**), the solid arrow represents the orientation of the HK and the dashed arrow represents an alternate orientation of the HK. Schematic representation of the domain orientations for the Pr homodimer (**D**), the Pr/Pfr heterodimer (**E**) and the Pfr homodimer (**F**). The white median represents the dimer interface which separates the two subunits. Clockwise rotation angles are displayed for each domain. The alternate orientation of the HK in the Pfr conformation is shown by an additional light blue panel in (**F**). The structures of the linkers that connect the PHY and the HK domains are shown in bright yellow for the Pr homodimer (**G**), the Pr/Pfr heterodimer (**H**) and the Pfr homodimer (**I**). The black arrows trace the axes of the linker helices. The displacement of the linker helix intersection is marked in (**G**) and (**H**). Kinks in the linker helix are marked for subunit A in the Pr/Pfr heterodimer (**H**) and

for both subunits in the homodimer of the Pfr state (**I**). (**I**) The linker helices in the homodimer of the Pr state are parallel to each other (black arrows).

Figure 7. Structural comparison of SaBphP2 with other BphPs. (**A**, **B**) Overlay of the Pr/Pfr heterodimers of SaBphP2 (blue ribbon) and the IsPadC (PDB code: 6ET7, yellow ribbon). (**A**) Equivalent subunits in Pr and Pfr state of each protein were compared, respectively. The overlay is marked Pr-Pr/Pfr-Pfr. The IsPadC heterodimer features a bent coiled coil linker (without a kink), that shifts the OM in the opposite direction compared to the SaBphP2. (**B**) The SaBphP2 subunit in the Pr state is overlayed with the IsPadC subunit in the Pfr state resulting in a better alignment of the linker region. The overlay is marked Pr-Pfr/Pfr-Pr. (**C**) The crystal structure of the DrBphP PCM in the Pfr state (PDB code: 4O01) shows a large opening of the PHY domains. (D) The cryo-EM SaBphP2 (orange) structure of the homodimer in the Pfr state is compared to the crystal structure of the PaBphP bathy phytochrome (PDB code: 3G6O, gray ribbon) in the dark-adapted Pfr state.

ScienceAdvances
AAAS

Supplementary Materials for

Photoreception and Signaling in Bacterial Phytochrome Revealed by Single Particle Cryo-EM

Marius Schmidt *et al.*

*Corresponding authors. Email: e-stojkovic@neiu.edu; smarius@uwm.edu

This PDF file includes:

Supplementary Methods and Results
Figs. S1 to S6
Table S1
Movie S1
References (1 to 6)

Supplementary Methods and Results

Cryo-EM Data analysis

A flow chart for single particle cryo-EM data analysis with *cryoSPARC* is shown in fig. S1. Starting from movies recorded by the electron microscope camera, the processing steps are described until the final structure is determined. Individual steps, results and details for the various SaBphP2 species are reported in the following. Processing and refinement statistics are shown for all species in table S1.

SaBphP2 cryo-EM maps and structures, overview

The structure of the full length SaBphP2 homodimer in the Pr state has been determined at an overall resolution of 4.13Å. The structure of the homodimer in the Pfr state has been determined at 3.75Å resolution. The cryo-EM map of the Pr/Pfr heterodimer is reconstructed at 3.75Å overall resolution. The local resolution in the PCM region of all three full-length SaBphP2 structures is around 3Å (fig. S1 – S3). The cryo-EM maps for a truncated SaBphP2 containing the PCM only were obtained at a resolution of ~4.5 Å. Data collection statistics for all species is shown in table S1. Fig. S5A compares chromophore structures observed in the cryo-EM maps of the Pr and Pfr species, and fig. S5B compares the analogous structures observed in crystals. Fig. S5C provides a view of the cryo-EM map looking down towards the HK effector domain. The map cannot be explained by a single HK structure. As a guide to the eye, two structures of HK domains (as determined from the Pr/Pfr heterodimer) were oriented into the map. The mutual orientation is shown by the arrows in analogy to the main text Fig. 6C. In fig. S6 details on the HK and the linker regions are reported. The HK is oriented differently from the Alphafold prediction (Figs. S6 a and S6 b). In fig. S6C the structure of the kink in the linker helix of subunit A is shown. Subunit A remains in the Pr conformation whereas subunit B is in the Pfr conformation. In fig. S6D both subunits are in the Pfr state and kinks are found in both subunits.

The cryo-EM structure of the full-length SaBphP2 Pr/Pfr heterodimer

The analysis of the cryo-EM data originating from the Pr/Pfr heterodimer is shown in the exemplary flowchart presented by fig. S1. The 17,880 raw movies were pre-processed with *patch motion correction* and *patch CTF estimation* jobs. The resulting micrographs were subjected to exposure curation from which 13,321 exposures were selected. The rest with poor CTF fits and large full-frame motions were eliminated. *Blob picking* was used to pick the initial lot of particles. Using 68,220 particles identified as full length phytochrome in 2D classification job, a low-resolution map at ~10 Å was generated with *ab-initio reconstruction*. The resulting map was used for template-based particle picking. This yielded approximately 270 particles per micrograph. Following an inspection of the particle picks, a total of 1,520,224 particles (box size 360 x 360 pixels) were extracted and averaged using the *2D classification* utility. High resolution classes were selected and subjected to further rounds of *2D classification.* Several rounds of particle curation resulted in a dataset with 865,248 particles. These particles were used by an *ab-initio reconstruction* job to generate five 3D maps without any reference (fig. S1). The five *ab-initio* classes were refined and the particles were classified amongst them with *heterogenous refinement*. The individual maps were refined to high-resolution and validated using the gold standard FSC with *nonuniform refinement*. Note: refinement in cryo-EM is distinct from crystallographic refinement. It means that individual images are re-oriented or re-examined using the initial, ab-initio 3D reconstruction as a template. A final map with best FSC resolution of 3.75 Å (fig. S1) was obtained with 215,374 particles.

The final cryo-EM map was interpreted with a structural model. The crystal structure of the PCM in the Pr state (*15*) fits reasonably well within subunit A of the cryo-EM map (Fig. 3A). The structure could be refined with minor adjustments. Subunit B, however, is in the Pfr state and the crystal structure do not fit. The Pfr structure determined here is quite different from the structures of other BphPs in the Pfr state. Several sections were identified in the Pr state where the secondary structures were conserved in the Pfr state as well. These sections were isolated from the crystal

structure and positioned individually in the the corresponding cryo-EM map sections. The remaining residues were manually built with *Coot (58)* and *ChimeraX (59)* as the side chains were clearly visible in the sharpened map produced by the *nonuniform refinement* job in *cryoSPARC*. The linker region was also modeled this way. Once an approximate model was obtained, real-space refinement in *Phenix (60)* was used to refine the model against the unsharpened map. To model the HK at a resolution of ~9 Å, its structure was predicted by *Alphafold (61)*. The orientations of the HK lobes in the *Alphafold* prediction do not agree with those observed in isolated HK crystal structures *(43)*. In the crystal structures the lobes are rotated by ~90° relative to the *Alphafold* prediction. The HK is connected to the dimer helices with a single stranded loop. Accordingly, each HK lobe in the *AlphaFold* prediction was rotated by 90°. The two possible orientations can be distinguished by the correlation factor between the structure and the cryo-EM map that becomes available after structural refinement. The correlation factor is 53 % for the *AlphaFold* solution and 65 % for the lobe orientations observed in the crystal structures (fig. S6A,B). The latter orientations were retained for a final structural refinement.

The cryo-EM structure of the full-length SaBphP2 homodimer in the Pr state

Processing steps are similar to those used to analyze the Pr/Pfr heterodimer dataset except that the heterodimer cryo-EM map was already available which was used immediately as a template for particle picking. Results are shown in fig. S2. A total of 1,112,759 particles were picked with the extraction box size of 400 x 400 pixels. These particles were filtered through multiple runs of *2D classification*. A set of 726,193 particles were used to reconstruct five *ab initio* maps. The best three maps were used as initial maps for *heterogenous refinement*. The map with best resolved features were used for further *homogenous* and non-*uniform refinement*. The final map with GSFSC resolution of 4.13 Å was obtained from 377,549 particles (fig. S2). The PCM region of subunit A of the hybrid structure was used to model the PCM region in both subunits. The coiled-coil linker was manually modeled in *Coot*. The overall structure was refined in *Phenix*.

The cryo-EM structure of the full-length SaBphP2 homodimer in the Pfr state

The dataset processing pipeline followed the same procedure as above. Starting with 2,217,983 particles picked (box size: 400 x 400 pixels) with template, a final map with GSFSC resolution of 3.75 Å (fig. S3) was obtained from 155,342 particles. The PCM region of subunit B in the heterodimer was used to model the PCM in both subunits of the Pfr homodimer. The coiled coil linker was manually modeled in *Coot* and refined in *Phenix*.

The cryo-EM structure of the truncated SaBphP2 PCM Pr/Pfr heterodimer

Since the dataset for the PCM Pr/Pfr heterodimer was collected in super resolution mode, an *output F-crop factor* of 1/2 was applied during the *Patch motion correction* job in *cryoSPARC*. For particle picking, a template was created using the PCM portion of the map obtained from the full-length heterodimer. A total of 2,903,962 particles were extracted using a smaller box size (compared to full-length dataset) of 256 x 256 pixels. The particles were filtered through multiple rounds of 2D classification. The final map with GSFSC resolution of 4.5 Å was obtained from 301,363 particles. The PCM structure extracted from the full-length heterodimer was used as an initial model for refinement in *Phenix*. The chromophore was omitted from the model prior to refinement. Results are shown in fig. S4A,B.

The cryo-EM structure of the truncated SaBphP2 PCM homodimer in the Pfr state

The dataset of the truncated SaBphP2 PCM was processed in the same way as the dataset of the respective full-length construct, since in both cases the movies were collected without the super resolution mode. The only difference was the particle extraction size which was set to 256 x 256 pixels. Starting with 3,616,004 particles, a final map was reconstructed from 276,639 particles at a GSFSC resolution of 4.61 Å. The PCM part of the full-length SaBphP2 Pfr homodimer was used as an initial model for refinement in *Phenix*. The BV chromophore was omitted from the model prior to refinement. Results are shown in fig. S4C,D.

Supplementary Figures

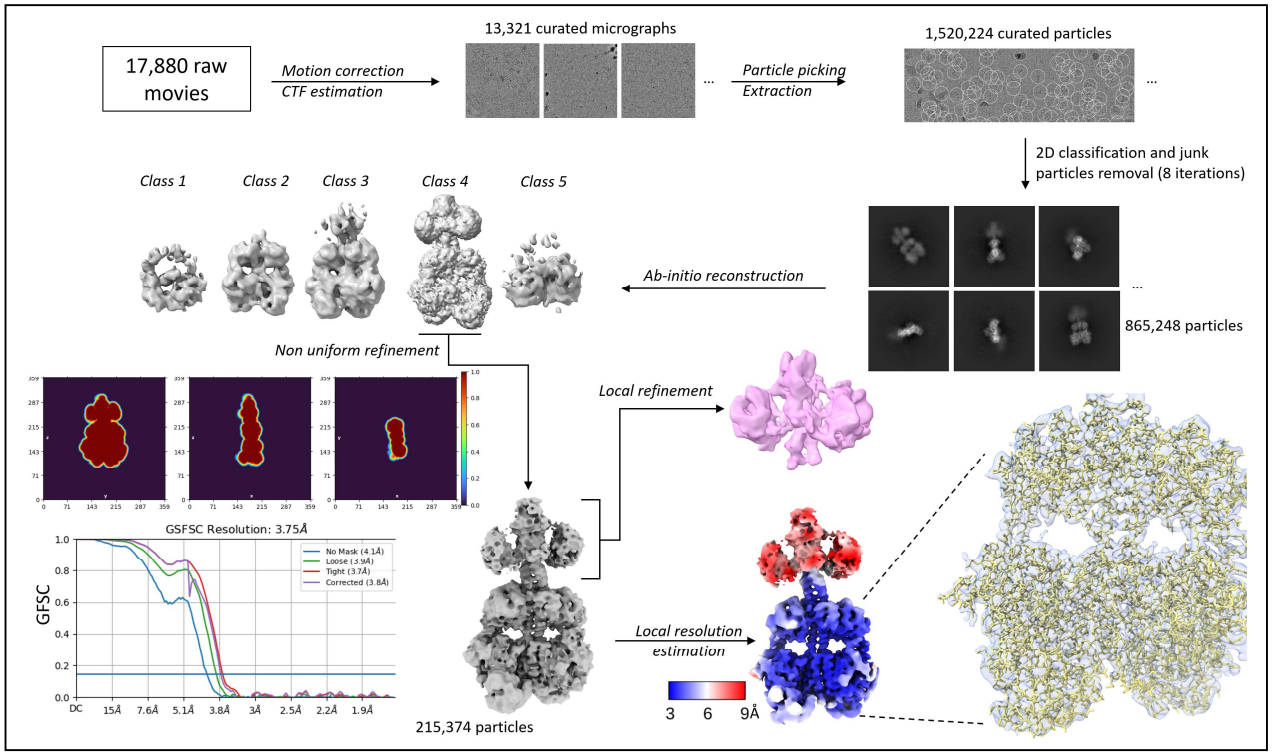

Figure S1. General flowchart and structure determination of the Pr/Pfr heterodimer. Cryo-EM structure determination with *cryoSPARC* is demonstrated using the full length SaBphP2 Pr/Pfr heterodimer as an example. From 17,880 camera movies 13,321 micrographs are extracted following motion correction and contrast transfer function (CTF) estimation. From these micrographs, particles were picked and a total of 1,520,224 curated particles were used for 2D classification jobs. Several iteration of 2D classification and particle sorting resulted in 865,248 particles that were used for map reconstruction. Five *ab initio* models were generated out of which the best representative model with 215,374 particles was selected for refinement. The map was updated by the non-uniform refinement utility without any symmetry applied. The refinement job informed the shape of the protein and the overall resolution of the reconstructed map. Local refinement was performed on the HK region of the map. The local resolution was estimated to determine the variability in the resolution across the map. A sharpened map was produced to model the atomic structure. The high resolution made it possible to model individual amino acids with their side chains in the PCM region.

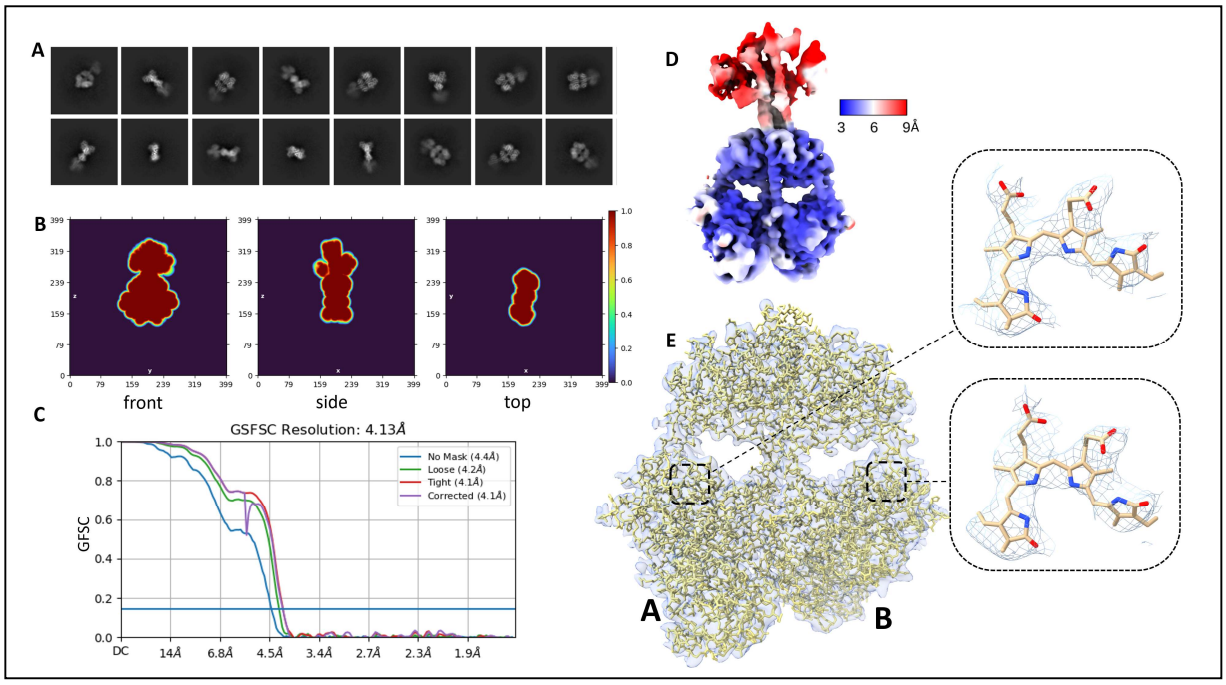

Figure S2. **Cryo-EM map reconstruction of the full-length SaBphP2 homodimer in the Pr state**. (**A**) Examples of 2D class averages of the particles, (**B**) a real space slice through the mask used for map refinement, (**C**) the gold standard Fourier shell correlation (GSFSC) resolution of the reconstructed EM map as reported by *cryoSPARC*, (**D**) resolution map of the reconstruction, (**E**) structural model of the SaBphP2 PCM including amino acid side chains as determined from the cryo-EM map. The cryo-EM densities of the BV chromophores in subunits A and B are enlarged.

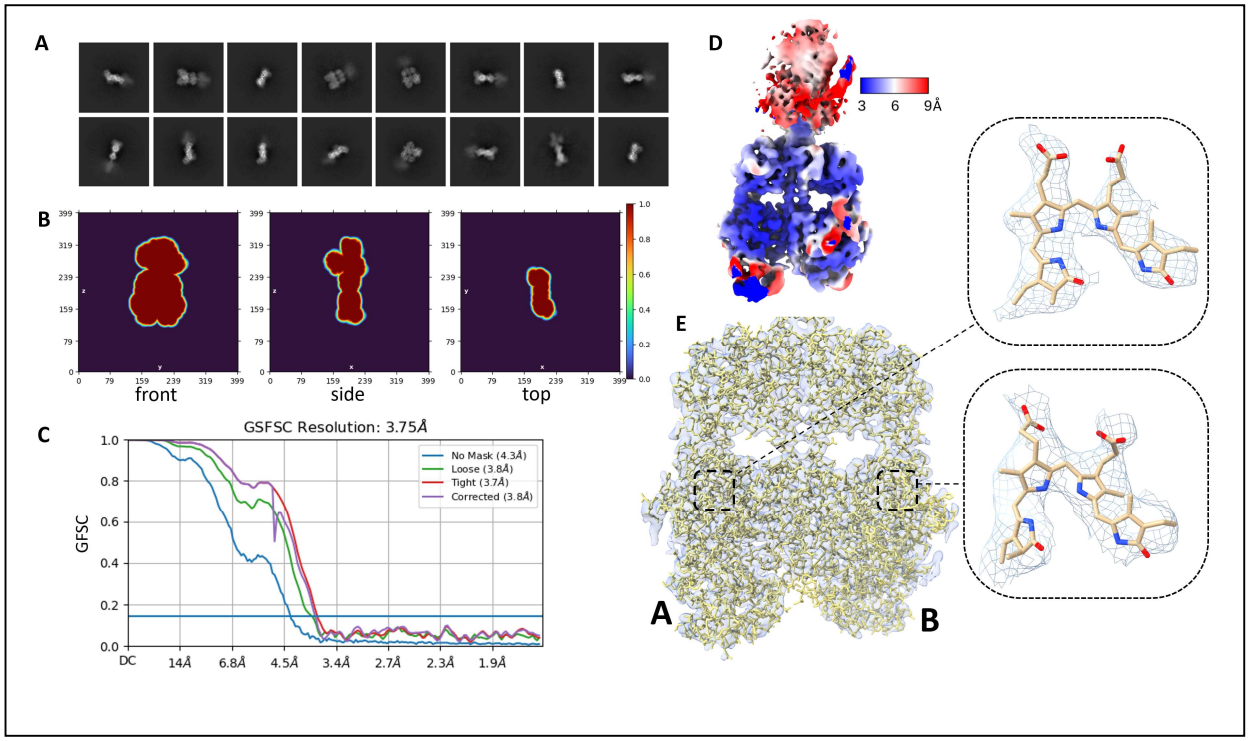

Figure S3. Cryo-EM map reconstruction of the full-length SaBphP2 homodimer in the Pfr state. (**A**) Examples of 2D class averages of the particles, (**B**) a real space slice through the mask used for map refinement, (**C**) the gold standard Fourier shell correlation (GSFSC) resolution of the reconstructed EM map as reported by *cryoSPARC*, (**D**) resolution map of the reconstruction, (**E**) structural model of the SaBphP2 PCM including amino acid side chains as determined from the cryo-EM map. The cryo-EM densities of the BV chromophores in subunits A and B are enlarged.

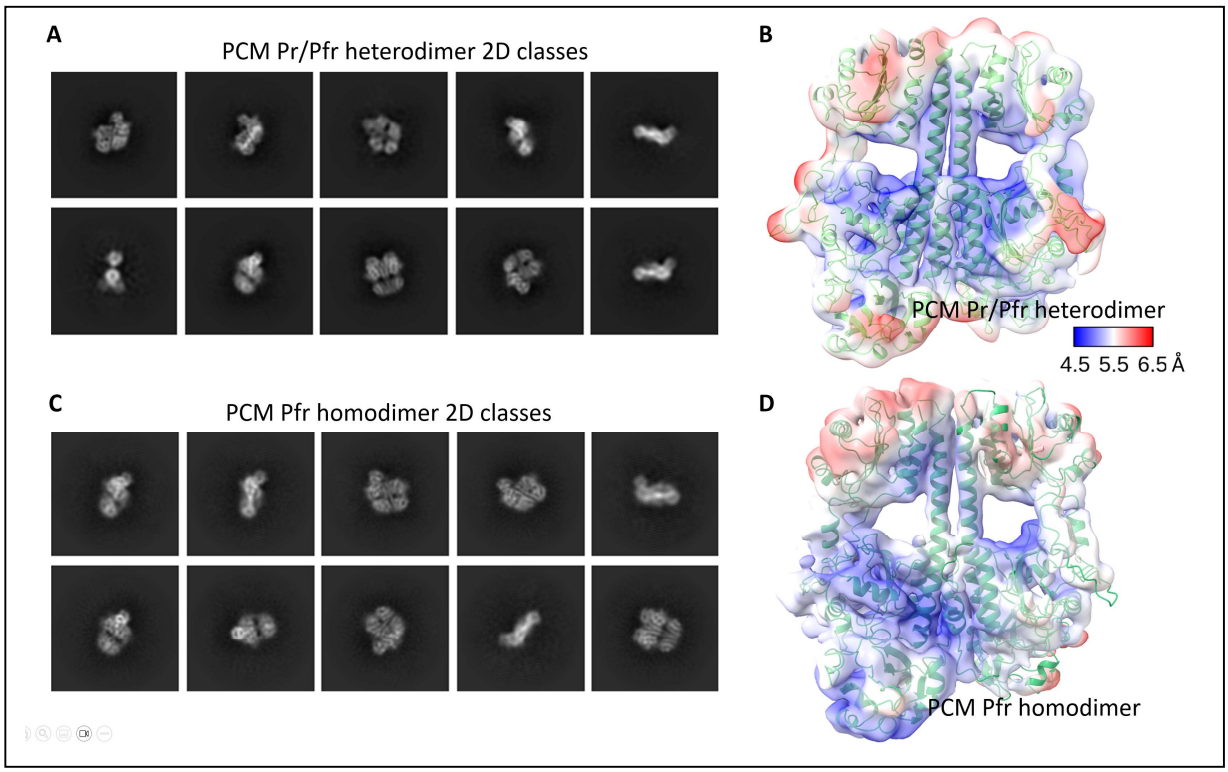

Figure S4. Cryo-EM structures of the short (truncated) SaBphP2 PCM construct. (**A**) Class averages of the the Pr/Pfr heterodimer, (**B**) resolution map of the reconstructed cryo-EM density, the low resolution backbone structure is shown in green. (**C**) Class averages of the homodimer in the Pfr state, (**D**) resolution map of the reconstructed cryo-EM density, the low resolution backbone structure is shown in green.

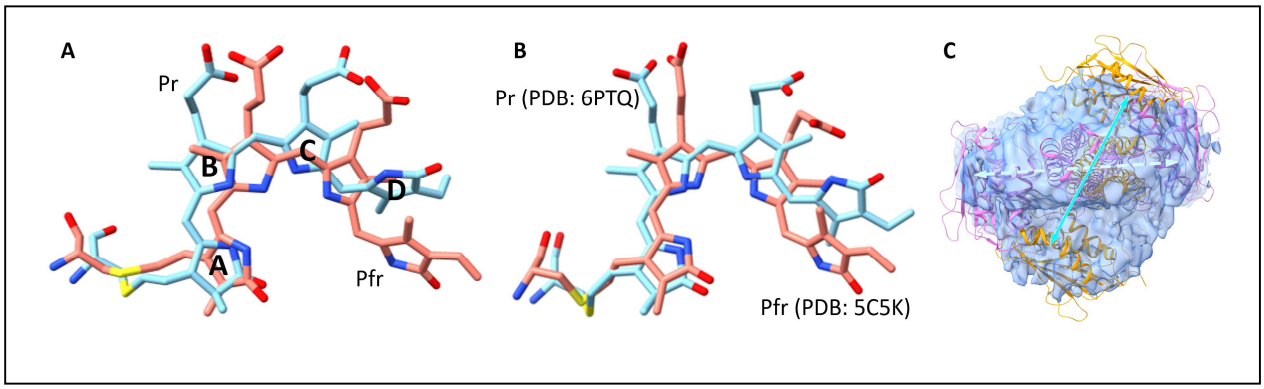

Figure S5. **Comparison of BV structures in the Pr and Pfr conformations.** (**A**) BV structures as determined by cryo-EM (this study). The BV ring D in the Z-configuration (blue) as found in the SaBphP2 PCM in the Pr state is overlayed on BV ring D in the *E*-configuration (salmon) found in the DrBphP PCM in the Pfr state. (**B**) Structures as determined from crystallography. Colors as in (A). Structures and structural changes are essentially the same between (**A**) and (**B**). Minor differences might arise due to relaxation restriction caused by crystal lattice constraints and/or caused by the lower resolution of the cyro-EM maps. (**C**) Low resolution cryo-EM map of the Pfr homodimer in the HK region (seen from the top). The map cannot be interpreted with a single structure. Magenta and yellow structures: HK structures as determined for the Pr/Pfr heterodimer were placed in two different orientations (magenta and orange) as a guide to the eye. The arrows (pale green and green) indicate the relative rotation of the two structures as also shown in Fig. 6C.

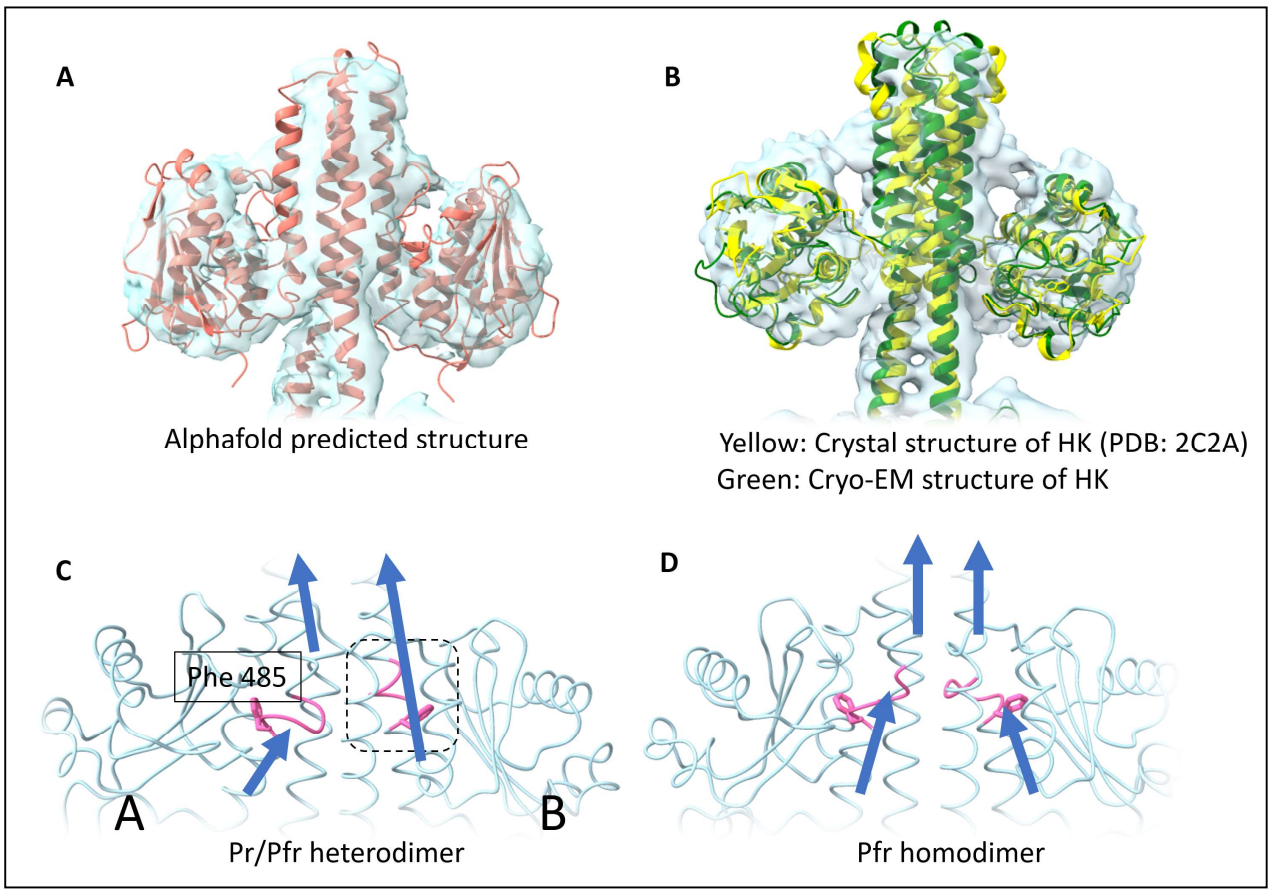

Figure S6. **Structure determination of the HK domain in the Pr/Pfr heterodimer and kink formation.** (**A**) The AlphaFold model (red ribbon) of the full length SaBphP2 (including the HK) is overlayed onto the cryo-EM map (blue) of the Pr/Pfr heterodimer. (**B**) The refined structural model of the full-length SaBphP2 (green ribbon) with the HK lobes rotated 90° relative to the AlphaFold model is overlayed on the structure of an isolated and unrelated HK (yellow, pdb-entry 2C2A). The cryo-EM map (blue) is shown in addition. The re-orientated HK lobes fit much better to the cryo-EM map and agree with those of the isolated HK lobes. (**C**) and (**D**): The kink regions in the linker in the Pr/Pfr heterodimer (C), and the homodimer in the Pfr state (D). (C) The helix around Phe485 (pink) melts and results in a kink of the helix in subunit A as a result of the Pr to Pfr transition in subunit B. The equivalent helical region in B is marked by a dashed box and shown in pink. (**D**) In the Pfr homodimer both helical regions around Phe485 unwind.

Supplementary Table

Tab. S1. Data collection and structural refinement statistics.

	Pr homodimer	**Pr/Pfr heterodimer**	**Pfr homodimer**	**PCM Pr/Pfr heterodimer**	**PCM Pfr homodimer**
Collection statistics					
Magnification			105,000x		
Voltage (kV)			300		
Electron exposure (e–/Å^2)	56.39	59.31	67.02	49.78	59.31
Pixel size (Å)		0.844		0.422	0.844
Initial particle images (no.)	1,112,759	1,520,224	2,217,983	2,903,962	3,616,004
Final particle images (no.)	377,549	215,374	155,342	301,361	276,639
Symmetry imposed			None		
Map resolution (Å)	4.13	3.75	3.75	4.5	4.61
FSC threshold			0.143		
Refinement statistics					
Refinement resolution (Å)	4.13	3.75	3.75	4.5	4.61
Model Composition					
Atoms	8250	10075	7759	7318	7318
Residues	1070	1478	1006	962	962
Ligands	2	2	2	0	0
B factors (Å^2)					
Protein	146.42	201.78	119.42	299.16	216.51
Ligand	179.65	129.74	154.74	n.a.	n.a.
RMS deviations					
Bond lengths (Å)	0.003	0.002	0.003	0.03	0.03
Bond angles (°)	0.76	0.547	0.898	0.837	0.865
Validation					
MolProbity score	1.76	1.75	2.03	2.35	2.24
Clash score	12.88	9.30	14.70	24.19	20.86
Ramachandran plot					
Favored (%)	97.27	96.19	94.88	92.38	93.42
Allowed (%)	2.45	3.74	4.82	7.62	6.47
Outliers (%)	0.28	0.07	0.30	0	0.1

Movies

Movie S1. The movie consists of three parts. In part (i) the structural changes near the chromophore regions are shown for the transition from the Pr to the Pfr state. The BV chromophore and the sensory tongue are marked. Part (ii) of the movie describes the overall structural changes observed during the Pr to Pfr transition. It also includes the structure of the Pr/Pfr heterodimer. In part (iii), cryo-EM map density changes in the HK region are shown. The cryo-EM map of the Pr/Pfr heterodimer is shown in addition to those of the homodimers in the Pr and Pfr states. The movie has been assembled by interpolation (morphing) between the different states. The perceived dynamics, therefore, should be regarded with caution as a guide to the eye.